Article

Sensory specializations drive octopus and squid behaviour

https://doi.org/10.1038/s41586-023-05808-z

Received: 2 September 2022

Accepted: 8 February 2023

Published online: 12 April 2023

Check for updates

Guipeun Kang[1,2,7], Corey A. H. Allard[3,7], Wendy A. Valencia-Montoya[3,4,5,7], Lena van Giesen[3], Jeong Joo Kim[1,2], Peter B. Kilian[3], Xiaochen Bai[1,2], Nicholas W. Bellono[3]✉ & Ryan E. Hibbs[1,2,6]✉

The evolution of new traits enables expansion into new ecological and behavioural niches. Nonetheless, demonstrated connections between divergence in protein structure, function and lineage-specific behaviours remain rare. Here we show that both octopus and squid use cephalopod-specific chemotactile receptors (CRs) to sense their respective marine environments, but structural adaptations in these receptors support the sensation of specific molecules suited to distinct physiological roles. We find that squid express ancient CRs that more closely resemble related nicotinic acetylcholine receptors, whereas octopuses exhibit a more recent expansion in CRs consistent with their elaborated 'taste by touch' sensory system. Using a combination of genetic profiling, physiology and behavioural analyses, we identify the founding member of squid CRs that detects soluble bitter molecules that are relevant in ambush predation. We present the cryo-electron microscopy structure of a squid CR and compare this with octopus CRs[1] and nicotinic receptors[2]. These analyses demonstrate an evolutionary transition from an ancestral aromatic 'cage' that coordinates soluble neurotransmitters or tastants to a more recent octopus CR hydrophobic binding pocket that traps insoluble molecules to mediate contact-dependent chemosensation. Thus, our study provides a foundation for understanding how adaptation of protein structure drives the diversification of organismal traits and behaviour.

Coleoid cephalopods, including octopus, squid and cuttlefish, are well-known for their large distributed nervous systems that enable advanced sensation and processing among their flexible arms. These evolutionary novelties support some of the most sophisticated behaviours observed among invertebrates, including voracious foraging using taste-by-touch chemotactile sensation. Octopuses have evolved specialized CRs in the suckers of their arms, which are used to explore hidden seafloor crevices for prey[1]. In octopus, CRs arose through gene duplication followed by divergence from ancestral nicotinic acetylcholine receptors[3]. Structural adaptations in CRs facilitate contact-dependent chemosensation of poorly soluble ligands such as terpenes, which are a diverse class of naturally occurring molecules produced by plants, fungi and bacteria, and often have a role in interspecies communication[4,5]. In contrast to octopus, squid and cuttlefish are ambush predators that strike and capture unsuspecting prey from a distance using their eight arms and two long tentacles[6] (Supplementary Videos 1 and 2). Here, we identify and analyse CRs from different cephalopods to uncover adaptative features suited to distinct predatory strategies. We then leveraged this unusual family of divergent sensory receptors to investigate principles of sensory system innovation. Using cryo-electron microscopy (cryo-EM) to determine the structure of the founding member of squid CRs, we compare CRs from squid and octopus with ancestral neurotransmitter receptors to reveal how subtle adaptations in protein structure support the evolution of novel lineage-specific traits and behaviour.

Squid CRs are bitter tastant receptors

As octopuses use contact-dependent chemosensation to find prey, we wondered whether squid might use arm chemoreception for their distinct ambush predation strategy. In contrast to octopuses (California two-spot octopus (*Octopus bimaculoides*)), squid (striped dumpling squid, *Sepioloidea lineolata*) suckers exhibit anatomical specializations including sharp hooks for capturing prey (Fig. 1a,b and Extended Data Fig. 1). These morphological adaptations complement visual predation from ambush positions in which squid hide or camouflage and rapidly strike unsuspecting prey from a distance, in contrast to active arm exploration demonstrated by octopus (Fig. 1b and Extended Data Fig. 1). In addition to their function in physical prey capture, suckers of squid arms and tentacles contain putative sensory cells, suggesting that they function as a sense organ[7] (Fig. 1b,c). Although such cells were rare in squid suckers compared with in octopus, electrophysiological analyses revealed that they similarly exhibited voltage-gated sodium and potassium currents, generated action potentials and responded to prey extracts (Fig. 1c,d and Extended Data Fig. 2). Consistent with a role for CRs in squid chemosensation, responses to prey extract were

[1]Department of Neuroscience, University of Texas Southwestern Medical Center, Dallas, TX, USA. [2]Department of Biophysics, University of Texas Southwestern Medical Center, Dallas, TX, USA. [3]Department of Molecular and Cellular Biology, Harvard University, Cambridge, MA, USA. [4]Department of Organismic and Evolutionary Biology, Harvard University, Cambridge, MA, USA. [5]Museum of Comparative Zoology, Harvard University, Cambridge, MA, USA. [6]Present address: Department of Neurobiology, University of California, San Diego, La Jolla, CA, USA. [7]These authors contributed equally: Guipeun Kang, Corey A. H. Allard, Wendy A. Valencia-Montoya. ✉e-mail: nbellono@harvard.edu; rehibbs@UCSD.EDU

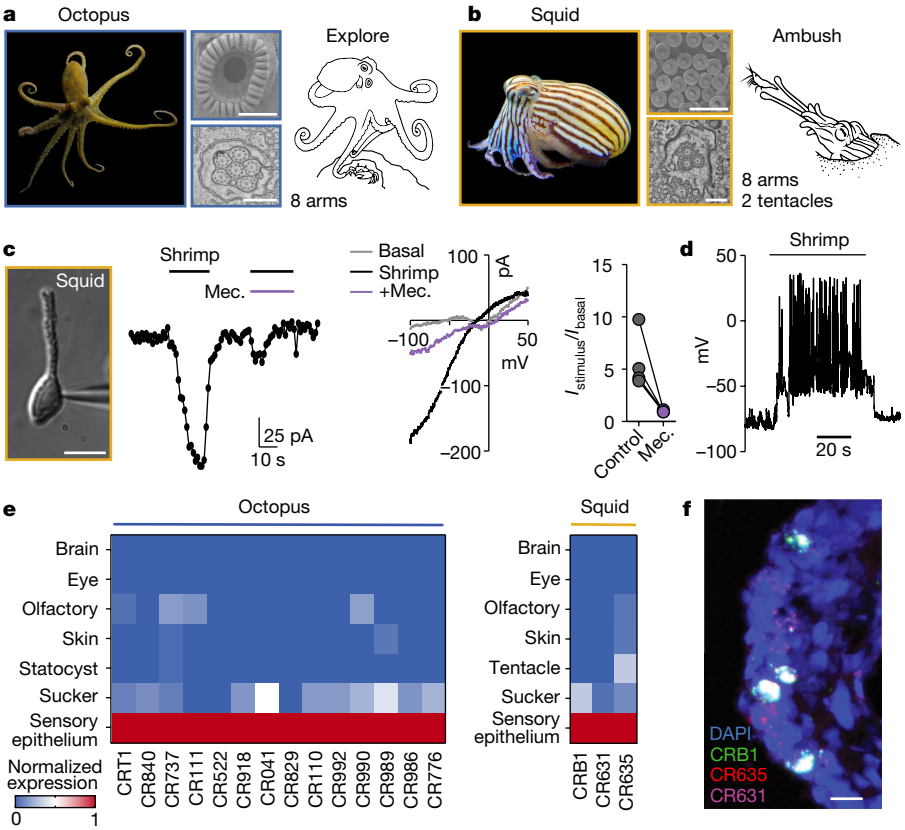

Fig. 1 | Squid express arm and tentacle CRs. a, Image of *O. bimaculoides* (left). Middle, octopuses have large smooth suckers with numerous ciliated receptor cells. Scale bars, 500 µm (top) and 200 nm (bottom). Right, octopuses use chemotactile taste-by-touch sensation for explorative predation. **b**, Image of *S. lineolata* (left). Middle, squid have rough spiked tentacle suckers with putative ciliated receptor cells. Scale bars, 500 µm (top) and 200 nm (bottom). Right, squid use ambush predation to strike and trap unsuspecting prey. **c**, Filtered shrimp extract (3 kDa) elicited mecamylamine (Mec.)-sensitive (1 mM) responses from chemosensory cells isolated from squid sucker sensory epithelium. $n = 4$ out of 8 responded. Statistical analysis was performed using a paired two-tailed Student's *t*-test; $P < 0.05$ (inhibition). Scale bar, 5 µm. **d**, Shrimp extract elicited action potentials in 3 out of 4 chemosensory cells. **e**, Octopus and squid CR mRNA transcripts were enriched in the sucker sensory epithelium relative to other sampled tissues. The colour scale shows transcripts per million normalized (norm.) to sensory epithelium. **f**, Squid CRs localized to the sensory epithelium, as visualized by RNAscope in situ hybridization. Representative of three animals. Nuclei were stained with DAPI (blue). Scale bar, 20 µm.

blocked by mecamylamine, an antagonist for octopus CRs[1] (Fig. 1c). To examine whether squid sensory cells express CRs, we generated transcriptomes from sucker sensory cells and other reference organs and compared with transcriptomic profiles from octopus tissues. In contrast to the 16 CRs expressed in octopus sucker sensory epithelia, we identified only three full-length CRs in squid sucker sensory cells, including chemotactile receptor for bitter tastants 1 (CRB1; Fig. 1e). CRB1 was the first characterized squid CR and was named for its robust sensitivity to bitter compounds (see below). As observed in octopus, squid CRs lacked key residues for acetylcholine binding, consistent with divergence from nicotinic receptors (Extended Data Fig. 3a and Supplementary Data 1). Furthermore, transcripts encoding distinct squid CRs colocalized within individual sensory cells in the squid arm and tentacle sucker epithelium, consistent with co-expression patterns observed in octopus CR cells[1] (Fig. 1f and Extended Data Fig. 3b). Although it is unclear whether squid CRs form heteromeric complexes, octopus CRs can co-assemble, a feature which may underlie the diversity of signals detected and transduced throughout the complex peripheral nervous system[1].

We next heterologously expressed squid CRs to examine whether they are sufficient to mediate chemosensory function. When expressed in HEK293 cells, CRB1 responded to prey extracts but not acetylcholine (Extended Data Fig. 3c). Consistent with octopus CRs and native sensory cells, squid CRB1 was activated by 3 kDa fish or shrimp extract, blocked by mecamylamine, and was insensitive to amino acids, sugars or amines—molecules that are commonly detected by olfactory or taste systems in other animals[8] (Fig. 2a and Extended Data Fig. 4c). In contrast to a representative octopus CR (CRT1, activated by hydrophobic molecules that facilitate touch-taste behaviour in octopus), squid CRB1 was insensitive to terpenes (Fig. 2a and Extended Data Fig. 3d). Instead, CRB1 robustly responded to the bitter compound denatonium and, to a lesser extent, to chloroquine (Fig. 2a). Similar to octopus CRs[1], CRB1 exhibited minimal desensitization with moderate pore block in response to high agonist concentration (Extended Data Fig. 3e). Importantly, denatonium elicited similar responses in native squid sensory cells, consistent with their expression of CRB1 (Fig. 2b). Furthermore, CRB1 activation by denatonium was specific to squid as octopus CRT1 was insensitive to denatonium (Fig. 2c).

Considering these results, we reasoned that CRB1 reflects a unique saliency of bitter chemicals to squid compared with octopus. To test this hypothesis, we recorded from axial nerves that innervate suckers of octopus and squid arms and tentacles. Amputated octopus arms responded to prey extracts and terpenes but did not respond to equivalent concentrations of denatonium (Fig. 2d and Extended Data Fig. 4a,c). Notably, isolated arms and tentacles from squid responded to prey extracts and terpenes, but also bitter molecules with robust neural activity, demonstrating that sensory encoding of bitter stimuli is unique to squid (Fig. 2d and Extended Data Fig. 4a,c). Consistent with conserved bitter sensation among squid, similar results were obtained

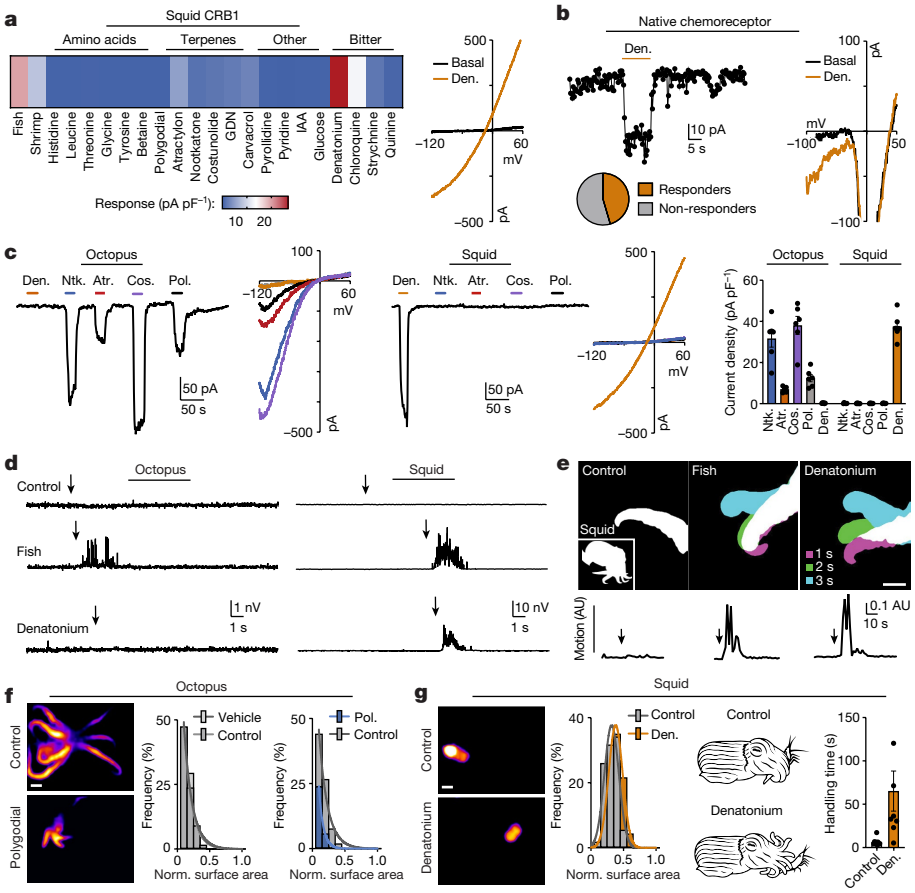

Fig. 2 | Squid use a bitter CR to taste by trap. a, Patch-clamp screen in HEK293 cells expressing squid CRB1 revealed sensitivity to the bitter tastant denatonium (Den.). $n = 3–8$ cells. 1 mM of tested compound. **b**, Native chemoreceptor cells were activated by 10 µM denatonium. $n = 5$ out of 11 cells. Atr., atractylon; Cos., costunolide; Ntk., nootkatone; Pol., polygodial. **c**, Squid CRB1 robustly responded to the bitter tastant denatonium but was insensitive to octopus CRT1 terpene agonists. $n = 6$ cells. Statistical analysis was performed using two-way analysis of variance (ANOVA) with post hoc Bonferroni test; $P < 0.0001$. **d**, Both octopus and squid arms responded to fish extract but only squid responded to 1 mM denatonium. $n = 3$ arms. Statistical analysis was performed using a two-tailed Student's *t*-test; $P < 0.05$ (denatonium versus sea water). **e**, Denatonium (1 mM) elicited robust autonomous movement in amputated squid arms and tentacles, but not in octopus arms (see also Extended Data Fig. 4). $n = 3$ arms. Statistical analysis was performed using a two-tailed Student's *t*-test; $P < 0.05$ (denatonium versus control). Scale bar, 3 cm. **f**, Octopuses used taste by touch to differentially explore terpene agonist (polygodial)-infused (100 µM) surfaces. $n = 18$ octopus and 8 squid trials. Statistical analysis was performed using a two-tailed Student's *t*-test; $P < 0.001$ (octopus touch number and duration in polygodial versus control). Scale bar, 3 cm. **g**, Squid did not explore infused surfaces in a denatonium-dependent manner, but differentially handled denatonium-covered (1 mM) shrimp after capturing with ambush predation. $n = 9$ trials. Statistical analysis was performed using a two-tailed Student's *t*-test; $P < 0.05$ (denatonium versus sea water). Scale bar, 3 cm. Data are mean ± s.e.m.

using longfin (*Doryteuthis pealeii*) and bobtail squid (*Euprymna berryi*) arms (Extended Data Fig. 4d,e). During nerve recordings, we noticed that agonists that elicited neural activity also produced robust autonomous arm and tentacle movement, emphasizing the behavioural relevance of these stimuli and the high degree of autonomy exhibited by cephalopod arms (Fig. 2e and Extended Data Fig. 4b,c). To examine whether bitter molecules elicited chemotactile responses in behaving squid, we added denatonium to the tank floor, similar to previous assays used to assess octopus chemotactile sensation[1]. Squid did not actively probe surfaces with their arms like octopus, consistent with their distinct ambush predation strategy (Fig. 2f, Extended Data Fig. 4f,g and Supplementary Videos 3 and 4). Instead, addition of denatonium to moulded agarose 'shrimp' significantly affected the amount of time that squid handled prey before consuming it (Fig. 2g). Occasionally, squid even rejected denatonium-soaked shrimp, which was not observed for control prey. Thus, the squid chemotactile sense appears more analogous to canonical taste by mediating the acceptance or rejection of captured prey after contacting arms, in contrast to benthic exploration by octopus.

CRB1 structural adaptations enable bitterant sensing

To probe how lineage-specific CRs sense distinct chemicals, we compared structural features of squid and octopus CRs and assessed how they diverge from ancestral nicotinic receptors. We first determined the structure of squid CRB1 in a complex with denatonium using single-particle cryo-EM (Fig. 3a–c and Extended Data Figs. 5 and 6). The CRB1 structure reached an overall resolution of 3.1 Å and revealed a general architecture common to the Cys-loop receptor superfamily. Each subunit of the pentameric complex comprises a large extracellular domain (ECD) and a transmembrane domain (TMD) that gives rise to a cation-permeable channel (Fig. 3a,b and Extended Data Figs. 5 and 6). The TMD channel is moderately asymmetric in both detergent and lipid nanodiscs (Extended Data Figs. 5, 7 and 8). The pore has a minimal diameter of 7 Å, consistent with expectations for a conducting state from permeation experiments and structures of related cationic Cys-loop receptors[2,9–12]. In the ECD, CRB1 has a unique disulfide bond that staples together the β8 and β9 strands, in turn connecting through a hydrophobic network to the conserved Cys-loop disulfide bond. This

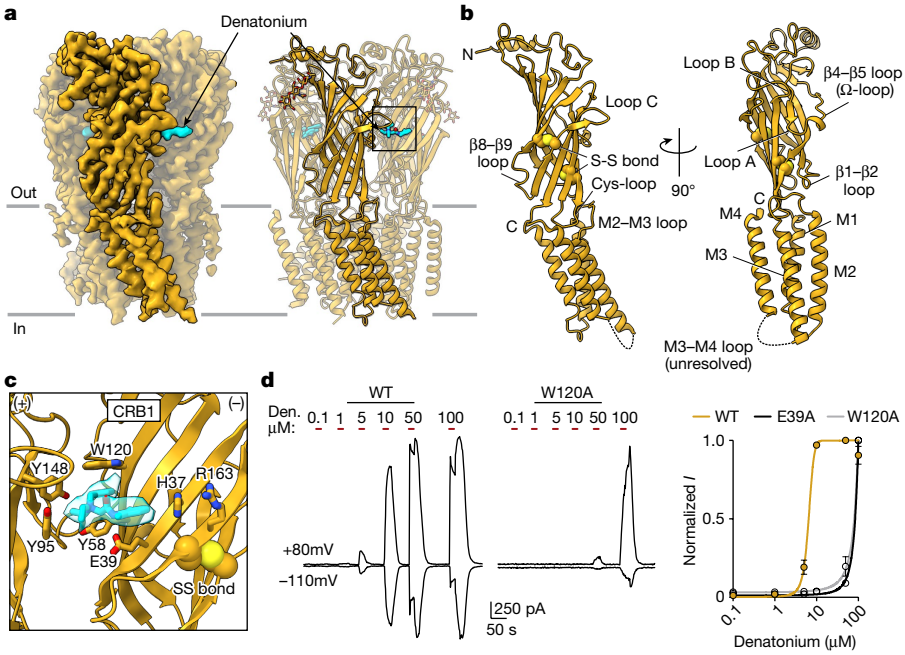

Fig. 3 | The structure of agonist-bound squid CRB1. a, Cryo-EM map and atomic model of squid CRB1 with a single subunit highlighted from the homopentamer and denatonium indicated in cyan. *N*-glycans and denatonium are shown as sticks. **b**, Single-subunit structure of squid CRB1 oriented as in **a** and rotated 90° about the pore axis. Disulfide bonds are shown as spheres. **c**, Details of the CRB1 agonist-binding site showing residues that are involved in denatonium binding as sticks. **d**, CRB1 ligand sensitivity was reduced by mutating residues that coordinate denatonium. Denatonium sensitivity (half-maximal effective concentration (EC_{50}) = 6.48 μM, 95% confidence interval = 5.70–7.25 μM) was decreased by the E39A and W120A mutations. $n = 8$ cells. Data are mean ± s.e.m.

set of interactions adds rigidity to the ECD, similar to the proposed role for the additional disulfide bond found in CRT1 (Extended Data Fig. 9). While both organisms' receptors have an additional disulfide, they are in different locations, suggesting convergent evolution after the split from nicotinic receptors. In CRB1, density corresponding to denatonium was resolved at subunit interfaces in a region overlapping with the agonist-binding sites of nicotinic receptors and CRT1 (Fig. 3c and Extended Data Fig. 6a,b). Compared with the α7 nicotinic receptor, squid CRB1 has a shorter loop C and is missing a key disulfide bond and tyrosine residues, features that are consistent with the insensitivity of CRB1 to acetylcholine (Extended Data Fig. 3c). However, reminiscent of the neurotransmitter-binding interface of nicotinic receptors, denatonium sits in an aromatic cage in concert with a glutamate positioned to form an electrostatic interaction with the amide group of denatonium[13] (Fig. 3c and Supplementary Video 5). Mutation of this glutamate (Glu39) or a tryptophan (Trp120) forming the roof of the cage resulted in a substantial reduction in receptor sensitivity to denatonium (Fig. 3d). Thus, CRB1 shares general structural features with ancestral nicotinic receptors but is specialized as a bitter tastant receptor through adaptation in key regions, especially the agonist-binding site.

Diversification of CRs for distinct sensory roles

Genomic and transcriptomic analyses demonstrate that nicotinic receptors have broadly expanded in molluscs, often in tandem arrays of intronless genes[14]. Among these expansions, we define CRs as the most derived clade containing CRB1 and CRT1, therefore defining a functional role for this lineage as peripheral sensory receptors. CRs are intronless, rapidly evolving and present only among analysed coleoid cephalopods (octopus, squid and cuttlefish), but absent in nautiloids and other molluscs[3,15,16] (Fig. 4a and Extended Data Fig. 10a). Thus, the evolution and expansion of CRs from nicotinic receptors coincides with diverse coleoid morphological novelties, elaborate neural architecture and sophisticated behaviour associated with the emergence of suckers and complex arms. Indeed, we find that CRs diverged from nicotinic receptors early in the course of cephalopod adaptive radiation (around 300 million years ago) to form three key subfamilies that cluster both in sequence homology and lineage specificity (Fig. 4a and Extended Data Fig. 10): CRB for bitterants; CRT for terpenes; and CRX for orphan receptors (Fig. 4b). CRBs are uniquely found in Decapodiformes (squid and cuttlefish), CRX receptors are specific to Octopodiformes (octopus) and CRTs are present in both lineages and are over-represented in octopus. Thus, restricted CR expression reflects physiological properties, notably squid-specific bitter sensation. To estimate the diversification times of the major CR subfamily members, we measured codon degeneracy between CR sequences and found that the Decapodiformes-specific CRB subfamily is the most ancient (Fig. 4b and Extended Data Fig. 10). This finding is consistent with structural similarities between CRB1 and nicotinic receptors, and the broad expansion of CR subtypes in octopus versus earlier divergent squid.

Comparison of squid and octopus CRs together with nicotinic receptor structures supports this molecular history—broadly, CR structural evolution is characterized by conservation of global receptor architecture and ionotropic function, with adaption occurring primarily in a common ligand-binding site. CRs share key features, including oligomerization, binding-site location and a relatively conserved ion permeation pathway (Extended Data Fig. 7). Both CR structures with agonists bound adopt putative activated, conducting states, consistent with the lack of substantial desensitization in electrophysiology experiments. In CRs, as in α7, a key negatively charged residue in the outer vestibule Ω loop[17] forms a constriction point that influences ion permeability and conductance (Extended Data Fig. 7). Examination of the ligand-binding pocket suggests that CRB1 represents a structural intermediate between nicotinic receptors and more differentiated octopus CRs, thereby reflecting CR evolutionary divergence. CRB1 preserves a notable feature found in the classical neurotransmitter site of nicotinic receptors: while in a slightly different region compared with nicotinic receptors, CRB1 uses a 'cage' of aromatic residues surrounding

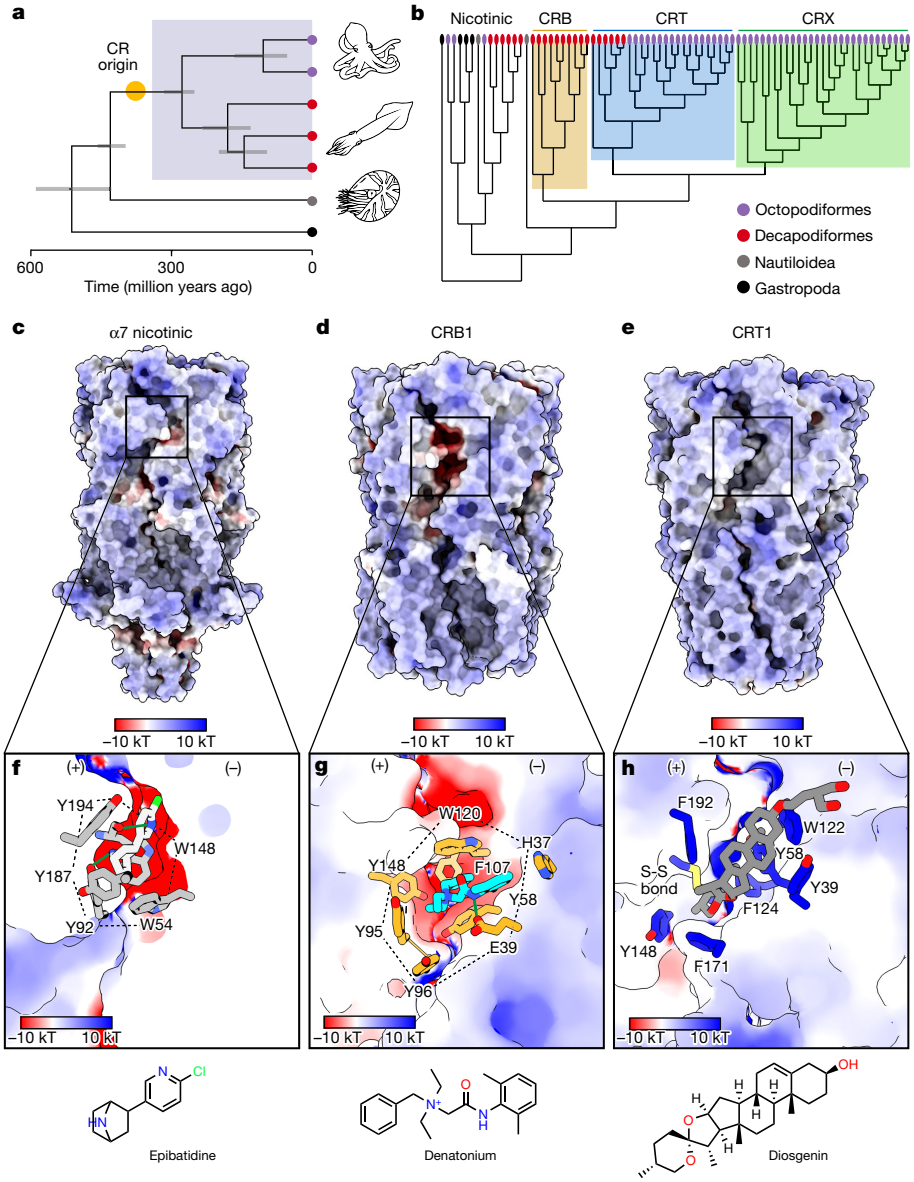

Fig. 4 | Structural specializations underlie an evolutionary transition from neurotransmission to distinct chemotactile sensory functions. **a**, Time-calibrated phylogeny of Cephalopoda inferred from whole mitochondrion genomes, including *L. gigantea* as an outgroup. Blue shading highlights coleoid cephalopods (octopus, squid, cuttlefish) and the inferred origin of CR sensory receptors at the base of this clade. Node bars (blue) indicate 95% confidence intervals for divergence time estimates at nodes. **b**, A phylogenetic tree of nicotinic acetylcholine-receptor-like proteins from Octopodiformes (*O. bimaculoides* and *O. sinensis*); Decapodiformes (*S. lineolata*, *D. pealeii*, *E. berryi*); nautiloids (*Nautilus pompilius*); and gastropods (*Lottia gigantea*) shows that CRs diverged from acetylcholine-like receptors, are unique to coleoid cephalopods, and comprise three major lineages: CRB (CR-bitter), CRT (CR-terpenes) and CRX (CR with unknown ligands). **c**–**e**, Side view of α7 (**c**), CRB1 (**d**) and CRT1 (**e**) coloured by Coulombic electrostatic potential; negatively and positively charged surfaces are coloured in red and blue, respectively. The black boxes indicate the orthosteric binding site. **f**, Details of the α7 nicotinic receptor neurotransmitter site with the agonist epibatidine bound. Aromatic residues near epibatidine (<5 Å) are shown as sticks. Interactions between epibatidine and carbonyl oxygen (Trp148) or hydroxyl oxygen (Tyr187) are shown as green lines. **g**, Details of CRB1 agonist-binding site with aromatic or charged residues near denatonium (<5 Å) shown as sticks. The green line indicates an electrostatic interaction between denatonium and Glu39. The black dotted lines in **f** and **g** indicate residues that form an aromatic cage in α7 and CRB1. **h**, Details of CRT1 agonist site with aromatic residues near diosgenin (<5 Å) shown as sticks.

a ligand that contains a basic nitrogen (Fig. 4c–h). The agonist-binding cage of α7 is highly hydrophilic; epibatidine is tucked in by a long loop C and stabilized by cation-π and electrostatic interactions (Fig. 4c–h). In CRB1, aromatic residues combine with a unique electrostatic interaction to form a structurally distinct cage suited to coordinate the bitter tastant denatonium. In the more derived octopus CRT1, the extensive hydrogen bonding network between β strands observed in CRB1 is disrupted and abolishes the cage structure (Fig. 4c–h and Extended Data Fig. 9). Instead, CRT1 Tyr166 in the β8 strand extends between β9 and β10, thereby breaking hydrogen bonds and tilting loop C upwards to form a more open pocket (Extended Data Fig. 9d,g). This flatter surface enables the accessibility of larger hydrophobic molecules such as terpenes implicated in octopus taste-by-touch chemotactile sensation (Fig. 4c–h). Thus, after expansion and evolution of CRs across species, structural features appear to diverge in the ECD to drive new function.

Collectively, our analyses provide a framework for understanding the molecular origins of new organismal traits. We demonstrate that cephalopod CRs are a unique innovation that arose though two key

steps: CR evolution involved (1) adaptation of an ancestral neurotransmitter receptor to a sensory role; and (2) duplication and specialization through structural modification of specific functional regions that is associated with lineage-specific behaviour. As a critical interface between ecological niche, complex neural processing and sophisticated behaviour, CRs represent a key innovation in cephalopod evolution. Indeed, numerous biological novelties arose in concert to synergistically drive morphological and functional specializations in octopus and squid. These adaptations are supported by an elaborate nervous system that is comparable in size to complex vertebrates, but with radically different organization. Thus, cephalopods provide notable examples of convergent and divergent evolution that can be exploited to understand the molecular basis of novelty across levels of biological organization.

Online content

Any methods, additional references, Nature Portfolio reporting summaries, source data, extended data, supplementary information, acknowledgements, peer review information; details of author contributions and competing interests; and statements of data and code availability are available at https://doi.org/10.1038/s41586-023-05808-z.

1. van Giesen, L., Kilian, P. B., Allard, C. A. H. & Bellono, N. W. Molecular basis of chemotactile sensation in octopus. *Cell* **183**, 594–604.e14 (2020).
2. Noviello, C. M. et al. Structure and gating mechanism of the α7 nicotinic acetylcholine receptor. *Cell* **184**, 2121–2134 (2021).
3. Albertin, C. B. et al. The octopus genome and the evolution of cephalopod neural and morphological novelties. *Nature* **524**, 220–224 (2015).
4. Mollo, E., Garson, M. J., Polese, G., Amodeo, P. & Ghiselin, M. T. Taste and smell in aquatic and terrestrial environments. *Nat. Prod. Rep.* **34**, 496–513 (2017).
5. Mollo, E. et al. Sensing marine biomolecules: smell, taste, and the evolutionary transition from aquatic to terrestrial life. *Front. Chem.* **2**, 92 (2014).
6. Hanlon, R. T. & Messenger, J. B. *Cephalopod Behaviour* (Univ. Cambridge, 1996).
7. Graziadei, P. Receptors in the sucker of the cuttlefish. *Nature* **203**, 384–387 (1964).
8. Bargmann, C. I. Comparative chemosensation from receptors to ecology. *Nature* **444**, 295–301 (2006).
9. Basak, S., Gicheru, Y., Rao, S., Sansom, M. S. P. & Chakrapani, S. Cryo-EM reveals two distinct serotonin-bound conformations of full-length 5-HT3A receptor. *Nature* **563**, 270–274 (2018).
10. Dwyer, T. M., Adams, D. J. & Hille, B. The permeability of the endplate channel to organic cations in frog muscle. *J. Gen. Physiol.* **75**, 469–492 (1980).
11. Polovinkin, L. et al. Conformational transitions of the serotonin 5-HT3 receptor. *Nature* **563**, 275–279 (2018).
12. Zhang, Y. et al. Asymmetric opening of the homopentameric 5-HT3A serotonin receptor in lipid bilayers. *Nat. Commun.* **12**, 1074 (2021).
13. Brejc, K. et al. Crystal structure of an ACh-binding protein reveals the ligand-binding domain of nicotinic receptors. *Nature* **411**, 269–276 (2001).
14. Jiao, Y., Cao, Y., Zheng, Z., Liu, M. & Guo, X. Massive expansion and diversity of nicotinic acetylcholine receptors in lophotrochozoans. *BMC Genom.* **20**, 937 (2019).
15. Albertin, C. B. et al. Genome and transcriptome mechanisms driving cephalopod evolution. *Nat. Commun.* **13**, 2427 (2022).
16. Zhang, Y. et al. The genome of *Nautilus pompilius* illuminates eye evolution and biomineralization. *Nat. Ecol. Evol.* **5**, 927–938 (2021).
17. Brams, M. et al. Modulation of the *Erwinia* ligand-gated ion channel (ELIC) and the 5-HT3 receptor via a common vestibule site. *eLife* **9**, e51511 (2020).

Methods

Animals

Adult California two-spot octopuses (*O. bimaculoides*) were wild-caught male and female adults (aged 1–2 years, Aquatic Research Consultants) and fed daily with fiddler crabs (*Leptuca pugilator*, Northeast Brine Shrimp). Adult (aged 1–2 years) striped dumpling squid (*S. lineolata*) and hummingbird bobtail squid (*E. berryi*) were laboratory cultured (Marine Biological Laboratories) and fed twice daily with grass shrimp (*Palaemonetes pugio*, Aquatic Indicators). Adult (aged 1–2 years) Longfin inshore squid (*D. pealeii*) were wild caught by jigging at the MBL, transported in aerated coolers to Harvard University and euthanized using established methods with immersion of 3.5% $MgCl_2$ and 15% ethanol followed by pithing for physiology and RNA extraction. All housed animals were kept under a 12 h–12 h light–dark cycle in filtered natural sea water. Animal protocols were approved by the Harvard University Animal Care and Use Committee (protocol ID 18-05-325) with further guidance from the Marine Biological Laboratories Marine Resource Center.

Cell culture

HEK293 cells (ATCC, authenticated and validated as negative for mycoplasma by the vendor) were cultured in Dulbecco's modified Eagle's medium (DMEM) (Gibco) supplemented with 10% fetal calf serum (Gibco) and 50 IU ml^{-1} penicillin and 50 μg ml^{-1} streptomycin (Gibco) at 37 °C, 5% CO_2 using standard techniques. For transfection, HEK293 cells were washed with Opti-MEM Reduced Serum Media (Gibco) and incubated with transfection mix containing 1 μg total of the indicated plasmid DNA and 3 μl Lipofectamine 3000 Transfection Reagent (Invitrogen) in Opti-MEM for 4–8 h at 37 °C. Cells were then replated onto glass coverslips in DMEM, incubated for 2 h at 37 °C and then incubated overnight at 30 °C.

CR construct, expression and purification

The full-length *CRB1* gene with a C-terminal strep-tag preceded by an SA linker was subcloned into the pEZT Bacmam expression vector[18]. Next, CRB1 Bacmam virus was produced and titrated as described previously[18] from Sf9 cells (ATCC, CRL-1711) for large-scale protein expression. Then, 4.8 l of suspension HEK293S GnTI$^-$ (ATCC CRL-3022) cells was grown at 37 °C and 8% CO_2 until they reached a cell density of around 4×10^6 cells per ml. Sodium butyrate (3 mM; Sigma-Aldrich) and viruses were added to the culture during transduction. The temperature was decreased to 30 °C after transducing expression with a multiplicity of infection (MOI) of 0.5. Transduced cells were collected after 72 h by centrifugation, resuspended in a TBS buffer (20 mM Tris, 150 mM NaCl, pH 7,4) containing 1 mM phenylmethanesulfonyl fluoride (Sigma-Aldrich), then lysed using an Avestin Emulsiflex. Lysed cells were centrifuged for 20 min at 10,000*g*, and the supernatant was collected and centrifuged again for 2 h at 186,000*g*. Membrane pellets were mechanically homogenized and solubilized for 1 h at 4 °C using a homogenizer with TBS buffer with 40 mM *n*-dodecyl-β-D-maltoside (DDM, Anatrace). Solubilized membranes were centrifuged for 40 min at 186,000*g*, then slowly passed over high-capacity Strep-Tactin (IBA) affinity resin at flow rate of 0.8 ml min^{-1}. The resin was washed with TBS buffer containing 0.1 mM glycol-diosgenin (GDN, Anatrace) then eluted with wash buffer supplemented with 5 mM desthiobiotin (Sigma-Aldrich) and 100 μM denatonium. After affinity chromatography, the eluted fractions were combined, concentrated and then centrifuged for 20 min at 40,000 rpm to remove aggregates before size-exclusion chromatography (SEC). The resulting supernatant was separated by SEC using the Superose 6 Increase 10/300 GL column (GE) equilibrated in TBS buffer containing 0.1 mM GDN. SEC fractions were pooled and concentrated, and the quality of purified receptor was assessed by analytical SEC before freezing the grids.

Cryo-EM sample preparation and single-particle cryo-EM data acquisition

A total of 3 μl of concentrated receptor protein ($A_{280} \approx 7.5$) was applied to copper R1.2/1.3 200 mesh holey carbon grids (Quantifoil) that were glow-discharged at 30 mA for 80 s. The grids were immediately blotted for 3 s under 100% humidity and 4 °C conditions, and then plunge-frozen into liquid ethane cooled by liquid nitrogen using the Vitrobot Mark IV (Thermo Fisher Scientific).

Cryo-EM samples were screened on the Talos Arctica system at UT Southwestern Medical Center and large dataset collection was performed at the Pacific Northwest Center for Cryo-EM (PNCC). Micrographs were collected on the 300 kV Titan Krios equipped with a K3 direct-electron detector (Gatan) and a GIF quantum energy filter (20 eV) in super-resolution mode. Images were collected with total electron dose of 50 $e^- Å^{-2}$ over 50 frames and a defocus range of −0.5 μm to −2.5 μm.

Single-particle cryo-EM data processing

Data processing was performed by following a general Relion 3.1 workflow[19]. Dose-fractionated images were gain-normalized, Fourier binned twice, aligned, dose-weighted and summed using MotionCor2[20]. The contrast transfer function correction and defocus values were estimated using GCTF[21]. Particles were automatically picked using crYOLO[22], and then processed for 2D classification to remove junk particles. A 3D reconstructed map generated from a small subset of particles was used as a reference (low-pass filtered to 30 Å) for the first round of 3D classification using C_1 symmetry. The two resulting good 3D classes were selected separately, and a second round of 3D classification was performed for each particle class. Before combining good 3D classes from the second round of 3D classification, the 3D maps were manually rotated to align with a reference class (class 1) using UCSF Chimera[23] to obtain the highest correlation between two maps. Once we determined the rotation angle of each 3D class that resulted in subunits being superimposed, the particles from each 3D class were rotated by editing the angle rotation column in the particles. star file. The particle star files were then joined and processed for 3D refinement, with restricted angular searches. After 3D refinement, a third round of 3D classification with local angular search (restricted to 4 degrees) was run, and only one class was selected by carefully checking local TMD density. Then, 3D refinement, CTF refinement and final TMD-focused 3D classification yielded one best 3D class. The final 3D class was further refined with C_1 symmetry; subsequently, the resulting volume was locally sharpened in Relion[19] and its local resolution was estimated using ResMap[24], yielding a final reconstruction at 3.13 Å resolution. The map quality was evaluated using Phenix mtriage[25], and the resulting FSC curve is included in Extended Data Fig. 5. Software packages for structural biology were compiled by SBGrid[26]. Cryo-EM data are summarized in Extended Data Table 1.

Model building, refinement and validation

An initial homology model was generated using the SwissModel[27] server based on the α3 subunit of the α3β4 human nicotinic acetylcholine receptor (Protein Data Bank (PDB): 6PV7) and the α7 human nicotinic acetylcholine (PDB: 7KOO) for the M1M2 loop conformation. This model was fitted into the density map in UCSF Chimera[23], then manually adjusted in Coot[28]. Density for M4 helices was strong in only two subunits; modelling was performed first in these subunits then applied to the other subunits in which density was ambiguous. The chemical structure of denatonium and refinement restraints were generated using the Grade Web Server (Global Phasing). Subsequently, the model was iteratively refined by manual adjustment in Coot and global real space refinement in Phenix[29,30]. The stereochemical statistics of the final model, including Ramachandran analysis, were assessed using Molprobity[31], and the final refinement statistics, including model-map

correlation and half-maps, were calculated using comprehensive validation and mtriage in Phenix[29,30].

Figures and graphical illustration

UCSF Chimera[23], UCSF ChimeraX[32] and Pymol[33] were used for graphical illustration of protein structures and density maps in the figures. Protein sequences were retrieved from the UniProtKB database[34] and aligned using PROMALS3D[35]. Pore radius profiles were calculated using Hole[36] and plotted using GraphPad Prism v.9.2.0 for Windows. Root mean square deviation values were calculated using the MatchMaker and Align functions in Chimera. The hydrophobicity profile along the permeation pathway was calculated by CHAP[37]. The interface area and the solvation free energy of protein–protein and protein–ligand interactions were calculated using PDBePISA[38], and the solvent accessibility analysis of the ligand-binding pocket was performed using CASTp3.0[39].

Patch-clamp electrophysiology

Patch-clamp recordings were carried out at room temperature using a MultiClamp 700B amplifier (Axon Instruments) and digitized using a Digidata 1550B (Axon Instruments) interface and pClamp software (Axon Instruments). Whole-cell recording data were filtered at 1 kHz and sampled at 10 kHz. For native cell recordings, borosilicate glass pipettes were polished to 8–10 MΩ. The standard extracellular solution contained 430 mM NaCl, 10 mM KCl, 10 mM HEPES, 10 mM $CaCl_2$, 50 mM $MgCl_2$, pH 7.6. Two intracellular solutions were used for recording. Most experiments used a Cs^+-based solution to reduce K^+ currents (500 mM Cs^+ methanesulfonate, 4 mM $MgCl_2$, 10 mM HEPES, 30 mM sucrose, 10 mM CsEGTA, pH 7.6). To measure K^+ currents and membrane voltage, we used 500 mM K^+ gluconate, 10 mM HEPES, 10 mM sucrose, 4 mM $MgCl_2$, 10 mM KEGTA, pH 7.6. For whole-cell recordings in HEK293 cells, pipettes were 3–5 MΩ. The standard extracellular solution contained 140 mM NaCl, 5 mM KCl, 10 mM HEPES, 2 mM $CaCl_2$, 2 mM $MgCl_2$, pH 7.4. The intracellular solution contained 140 mM Cs^+ methanesulfonate, 1 mM $MgCl_2$, 5 mM NaCl, 10 mM CsEGTA, 10 mM HEPES, 10 mM sucrose, pH 7.2. In ion-substitution experiments, relative permeability was determined by measuring the shift in reversal potential (E_{rev}) after the substitution of equimolar monovalent cations. E_{rev} was extracted from voltage-ramp experiments as described for measuring agonist-elicited currents. The extracellular solution contained 150 mM Na^+, Cs, NMDG$^+$ or 100 mM Ca^{2+}, Mg^{2+} and intracellular solution contained 150 mM CsCl and 1 mM CsEGTA. Solutions were buffered with 10 mM HEPES. Permeability ratios were estimated using the Goldman–Hodgkin–Katz (GHK) equation: $P_X/P_{Na} = ([Na^+]_{Luminal}/[X]_{Cytoplasmic})(\exp(E_{rev}F/RT))$, $P_{Ca}/P_{Na} = (4[Ca^{2+}]_{Luminal}/[Na^+]_{Cytoplasmic})(\exp(E_{rev}F/RT))$, where P is permeability, X is the ion, F is the Faraday constant, R is the gas constant and T is the temperature.

The following pharmacological agents were used: 4-aminopyridine (Tocris, 0940), acetylcholine (Sigma-Aldrich, A6625), mecamylamine (Tocris, 2843), BAPTA (Tocris, 2786), Cd^{2+} (Sigma-Aldrich, 202908), tetrodotoxin (Tocris, 1078), nootkatone (Sigma-Aldrich, W316620), polygodial (Cayman Chemicals, 14979), atractylon (Carbosynth, FA74011), threonine, arginine, alanine, serine, leucine, glutamine, histidine and lysine (all Sigma-Aldrich), benzaldehyde (Sigma-Aldrich, 418099), 2-(diethylamino)ethanol (Sigma-Aldrich, 471321), isoamyl acetate (Sigma-Aldrich, 112674), sucrose (Sigma-Aldrich, S7903), pyridine (Thermo Fisher Scientific, 13178), 3-aminopyrrolidine (Sigma-Aldrich, 540781), triethylamine (Sigma-Aldrich, 471283), 2,5-dimethylpyrazine (Sigma-Aldrich, W327204), tyramine (Sigma-Aldrich), chloroquine (Sigma-Aldrich, C6628), denatonium benzoate (Sigma-Aldrich, D5765), carvacrol (Sigma-Aldrich, W224502), eucalyptol (Fluka, 46090), limonene (Sigma-Aldrich, 183164). Compounds were dissolved in water, ethanol (<1%) or DMSO (<1%). Natural products (fish, crab, ink) were flash-frozen, ground with mortar and pestle, and filtered with 3 kDa ultracentrifugal filters (Amicon UFC500324). Fractions were generated using C18 filters (Restek, 24051) using methanol and water to collect hydrophilic and hydrophobic fractions, respectively.

In native cells, agonist-elicited currents were measured during 100 ms voltage ramps from −120 to 80 mV applied every 1s, which were quantified at −110 mV. Agonist-evoked currents were measured at −110 mV during 500 ms ramps from −120 to 100 mV in HEK293. All time courses displayed currents measured at −110 mV during successive ramps. Inhibitory effects were quantified as differences in normalized peak current from the same cell after bath application of the drug ($I_{treatment}/I_{control}$) and agonists were quantified by increases in peak current versus basal ($I_{treatment}/I_{basal}$). For CRs and chemoreceptor cells, effects were quantified using currents measured at −110 mV. Desensitization and/or pore block was quantified at the end of agonist application versus peak current (I_{End}/I_{Peak}). Estimated EC_{50} and 95% confidence intervals were calculated from sigmoidal dose–response relationships established from normalizing agonist-evoked currents to those elicited by maximal concentrations in the same cell.

Voltage-gated currents were leak-subtracted online using a p/4 protocol, and membrane potentials were corrected for liquid junction potentials. Voltage-gated currents were measured in response to a 200 ms voltage pulse in 10 mV increments from a −110 mV holding potential. G–V relationships were derived from I–V curves by calculating G as follows: $G = I/(V_m - E_{rev})$ and fit with a Boltzmann equation; I is current, G is conductance and V_m is membrane voltage. Voltage-dependent inactivation was measured using test pulses to −10 mV (inward currents) or +60 mV (K^+ currents) voltage pulses after a series of 1 s pre-pulses ranging from −110 mV to +60 mV. Voltage-dependent inactivation was quantified as I/I_{max}, with I_{max} occurring at the voltage pulse after a −110 mV pre-pulse. Current kinetics were quantified using single exponential fits or the time to reach peak amplitude from activation. Voltage-dependent K^+ currents were isolated by including 1 µM TTX and 500 µM Cd^{2+} in the extracellular solution. In current-clamp recordings, resting membrane potential was measured without injecting current ($I = 0$). 1 s depolarizing current steps of various amplitudes were injected to measure spikes, which were quantified by frequency (spikes per second) or amplitude.

Two-electrode voltage clamp

Defolliculated oocytes were purchased from Ecocyte or Xenopus1 and stored in Modified Barth's Solution (88 mM NaCl, 1 mM KCl, 5 mM Tris-HCl, 1 mM $MgSO_4$, 0.4 mM $CaCl_2$, 0.33 mM $Ca(NO_3)_2$, 2.4 mM $NaHCO_3$, pH 7.4) supplemented with 0.1 mg ml^{-1} gentamycin for up to 1 week at 4 °C until use. For oocyte expression, plasmid DNA was linearized using Not1-HF (NEB, R3189) for 2 h at 37 °C. Linearized DNA was purified using a PCR purification Kit (Qiagen, 28104) and eluted in 30 ml RNase-free water. RNA synthesis was performed with 1–3 µg DNA using the mMessage mMachine T7 Transcription Kit including 15 min of DNase treatment (Ambion, AM1344). RNA was treated with the Zymo Clean & Concentrator Kit and aliquoted at a concentration of approximately 10 µg ml^{-1} for injection. Oocytes were injected with 25 ng RNA using the Nanoject III (Drummond scientific) and incubated in Modified Barth's Solution at 17 °C overnight. Two-electrode voltage recordings were carried out at room temperature with an Oocyte Clamp OC-725C amplifier (Warner Instruments) and digitized using a Digidata 1550B (Axon Instruments) interface and pClamp 11 software. Data were filtered at 1 kHz and sampled at 10 kHz. Recordings were performed using borosilicate glass pipettes with resistances of 7–10 MΩ when filled with 3 M KCl. All chemicals were diluted in ND96 extracellular solution (96 mM NaCl, 2 mM KCl, 5 mM HEPES, 1 mM $MgCl_2$, 2 mM $CaCl_2$ adjusted to pH 7.4 with NaOH). Insoluble chemicals were first reconstituted in DMSO, and then diluted in ND96 to 1% final DMSO. Stimulus-evoked currents were obtained using 200 ms voltage ramps from −120 mV to 120 mV applied every 500 ms with an interstimulus holding potential of −40 mV. Dose–response relationships were calculated using peak currents measured at −115 mV.

Histology

Arms or tentacles from the indicated species were fixed in 4% paraformaldehyde in PBS for approximately 16–24 h on a rocker. Appendages were then dissected into short lengthwise sections, washed three times with PBST (Triton X-100 0.1%) and incubated in 30% sucrose in PBST at 4 °C on ice. After embedding in optimal cutting temperature compound (OCT), the samples were frozen and sectioned using a cryostat (Leica, CM3050S) at a thickness of 35 µm. After subsequent washes in PBST, the samples were blocked for 1 h in 5% normal goat serum (NGS) in PBST and antibody solution containing anti-HRP-Cy3 (1:500) (Jackson Immuno, 123-545-021) was applied for 24 h at 4 °C in 5% NGS/PBST. Finally, the samples were washed 3–5 times in PBST, mounted in Vectashield with DAPI (Vector Laboratories) and imaged using the LSM 980 Confocal Microscope with Airyscan2 (Zeiss). Images were processed using FIJI.

In situ hybridization

Tissues were collected from live samples and suckers were immediately frozen in OCT. Sections (18 µM) were performed on fresh frozen tissue using a cryostat (Leica, CM3050S). Probes were designed by ACD and the manufacturer's recommended protocol was followed as described for fresh frozen tissues. Pretreat 3 was used for 30 min and the fluorescent probes used included TSA-FITC, TSA-Cy3 and TSA-Cy5 (Perkin Elmer, NEL744E001KT and NEL754001KT), samples were mounted in ProLong Gold (Thermo Fisher Scientific, P36931) with DAPI, and imaged using the LSM 980 Confocal Microscope with Airyscan2 (Zeiss). Images were processed using FIJI.

Electron microscopy

Scanning electron microscopy. The samples were fixed overnight in a mixture of 1.25% formaldehyde, 2.5% glutaraldehyde and 0.03% picric acid in 0.1 M sodium cacodylate buffer, pH 7.4. The fixed tissues were washed with 0.1 M sodium cacodylate buffer and post-fixed with 1% osmium tetroxide in 0.1 M sodium cacodylate buffer for 2 h. Tissues were then rinsed in double-distilled H_2O and dehydrated through a series of ethanol (30%, 50%, 70%, 95% and twice at 100%) for 15 min per solution. Dehydrated tissues were dried in an autosamdri-815 critical point dryer and mounted on aluminium stages with silver paint and coated with platinum (10 nm). The dried tissues were observed using the Hitachi S-4700 Field Emission Scanning Electron Microscope (FE-SEM) at an accelerating voltage of 5 kV. At least three tissue samples were analysed per animal.

TEM. Samples were fixed overnight in a mixture of 1.25% formaldehyde, 2.5% glutaraldehyde and 0.03% picric acid in 0.1 M sodium cacodylate buffer, pH 7.4. The fixed tissues were washed with 0.1 M sodium cacodylate buffer and post-fixed with 1% osmium tetroxide/1.5% potassium ferrocyanide (in H_2O) for 2 h. The samples were then washed in a maleate buffer and post-fixed in 1% uranyl acetate in maleate buffer for 1 h. Tissues were then rinsed in double-distilled H_2O and dehydrated through a series of ethanol (50%, 70%, 95% and twice at 100%) for 15 min per solution. Dehydrated tissues were put in propylene oxide for 5 min before they were infiltrated in epon mixed 1:1 with propylene oxide overnight at 4 °C. Samples were polymerized in a 60 °C oven in epon resin for 48 h. They were then sectioned into 80 nm thin sections and imaged on the JEOL 1200EX Transmission Electron Microscope. At least three tissue samples were analysed per animal.

Transcriptomics

We generated tissue-specific de novo transcriptomes for *S. lineolata*, *D. pealeii* and *E. berryi* (Supplementary Table 1). Tissues were dissected and stored frozen in RNAlater until use. RNA extraction, library preparation and RNA sequencing were performed by Genewiz (Azenta) using the HiSeq (2 × 150 bp) platform. For *O. bimaculoides*, we used a transcriptome that was previously assembled by our group (BioProject: PRJNA658966). We assembled additional transcriptomes for *Nautilus pompilius* (Sequence Read Archive: SRR11485678–SRR11485687) and *D. pealeii* (Sequence Read Archive: SRR18071805–SRR18071807, SRR18071791, SRR18071792, SRR18071794 and SRR18071795) from raw reads available in GenBank. Adaptor trimming was performed using trim galore, and reference transcriptomes were assembled de novo using Trinity[40]. Open reading frames were identified using transdecoder. Reads were pseudoaligned and transcript abundance was estimated using Kallisto[41] and our transcriptome assemblies as a reference. Annotation was performed using Diamond[42].

Phylogenetics and sequence divergence

To increase phylogenetic sampling and sequence representation, we used proteins predicted from the genomes of *O. sinensis* (BioProject: PRJNA541812), *N. pompilius* (BioProject: PRJNA614552) and *L. gigantea* (BioProject: PRJNA175706). We used these proteomes, along with the transcriptomes generated in this study and CRs annotated from the *D. pealeii* genome (BioProject: PRJNA641326) to mine for acetylcholine-receptor-like genes using the sequences of CRB1 (NCBI: OQ301567), CRT1 (NCBI: NW_014712376.1) and α7 receptor (NCBI: U40583.2) as templates for iterative search in jackHMMER[43] with an *e* value of 10×10^{-5}. Protein sequence annotations were confirmed using BLASTn[44] and clustered at 95% identity using CD-hit[45] to remove isoforms and duplicates. We aligned amino acid sequences with MAFFT (v.7)[46] and curated the alignments manually in Geneious Prime (v.2022.2; https://www.geneious.com) to obtain high-quality alignments. We used ModelFinder[47] to assess the best model of substitution for phylogenetic inference. We estimated maximum-likelihood trees in IQ-TREE (v.2.0)[48], conducting ten independent runs to ensure convergence and selected the tree with the highest likelihood. Support for clades was calculated using ultrafast bootstrap approximation UFBoot2[49].

We retrieved whole-mitochondrion genomes of *S. lineolata* (MW484944.1), *D. opalescens* (NC_012840.1), *E. berryi* (MW478823.1), *O. sinenesis* (NC_052881.1), *N. pompilius* (NC_035715.1) and *L. digitalis* (DQ238599.1) to infer a time-calibrated phylogeny of the species or placeholders included in the sequence analysis. Alignment and phylogenetic inference were performed as described above. We used MCMCtree (v.4.9)[50] for divergence time estimation, incorporating secondary node calibrations based on a recent fossil-calibrated phylogeny of mollusks[51]. The remaining node age priors were set to uniform. We conducted a likelihood approximation with the calculation of the gradient and Hessian matrix of the branch lengths to speed computation and ran the concatenated alignment under the F84 substitution model and gamma with five rate parameters. Tree visualization was implemented using the packages ggtree (v.3.4.2)[52] and phytools in R (v.4.2.1) and iTOL[53].

Fourfold degenerate site distances (4DTv) were estimated between all pairs of CR genes. Amino acid sequences were aligned using MAFFT and converted to codon alignments using Pal2Nal[54]. We identified fourfold degenerate sites and calculated their rate of transversion using a custom Python script.

Autonomous arm behaviour

Arm tips from sedated animals were transferred to a 10 cm Petri dish containing 50 ml sea water and held in place using suction through an appropriately sized tygon tube. Odorants were first dissolved in DMSO and then diluted in holding solution to 0.1–1% final DMSO. Then, 1 ml stimulus at the indicated concentration was perfused over the arm over 2 s using a micropipette. Arm behaviour was recorded using a FLIR grasshopper 3 camera (Teledyne) equipped with a 35 mm Nikon DX AF-S NIKKOR 1:1.8G lens (Nikon) at 500 ms intervals. Videos were segmented and motion was measured using ImageJ (NIH) by stack difference projections.

Axial nerve recording

Arm tips or tentacles from sedated animals were transferred to a 10 cm Petri dish containing 50 ml holding solution (430 mM NaCl, 10 mM KCl, 10 mM HEPES, 10 mM $CaCl_2$, 50 mM $MgCl_2$, 10 mM D-glucose, pH 7.6). Nerve recordings were performed using a borosilicate glass suction electrode shaped and polished to fit over the entire cut end of the radial nerve. A similar reference electrode was placed into the bath. Gap-free recordings were made with 10 kHz sampling at 10,000× gain, and signals were high-pass filtered at 100 Hz and low-pass filtered at 1 kHz using a Warner DP-311A headstage and AC/DC amplifier (Warner) and digitized using a Digidata 1440A digitizer (Molecular Devices) using ClampEx software (Molecular Devices). Recordings were processed using Clampfit (Molecular Devices). For quantification of responses, the absolute value of the signal was processed using a low-pass 25 Hz Gaussian filter, the baseline signal was subtracted and the response amplitude was integrated over the response area. For controls and stimuli for which no response was observed, a similar response area was measured as for arm agonists.

Animal behaviour

Light/dark octopus behaviour. Octopuses were placed in a ~190 l tank prepared in a room with full lighting control and filmed top-down with an infrared camera (SiOnyx Aurora) fitted with an 850 nm infrared filter (Neewer). The tank was illuminated both with overhead room lights and with a panel of SMD3528-300-IR infrared (850 nm) LED light strip lights. After a 10 min acclimation to the tank, the camera was activated and the animal was filmed for 30 s. The overhead room lights were then turned off and the room was made totally dark for an additional 30 s before turning the overhead lights back on. This was repeated twice with each octopus before ending the trial. Still images were extracted from the videos 2 s after the overhead lights were either turned on or turned off and imported into ImageJ. The outlines of the octopus's body 2 s after the incidence of full overhead light and 2 s after the incidence of total darkness were traced and converted into total pixel area, which was then converted into square inches using a known measurement to calibrate the ImageJ (NIH) measurement tool.

To measure predation, first, a fiddler crab was placed in a randomly determined corner of the tank in a 11 cm diameter, 5 cm tall glass dish. Then, an octopus was placed into a different, randomly determined corner of the tank. The camera was activated when the octopus was placed in the tank. Trials were filmed until the octopus had captured the crab (always less than 10 min). The condition of the trial (lights on versus lights off, and live crab versus dead crab) were also randomly determined. Dead crabs were killed by pithing the carapace from the seam between the top and bottom halves of the shell. A 'pounce' result was quantified as a distance response to prey and use of the siphon to swim over to the crab followed by stereotypic use of the arms and webbing to engulf the prey. A 'contact' result was quantified as no response to prey until the arm incidentally meets the shell of the crab through typical exploration of the tank space, which then results in the stereotypic use of the arms and webbing to engulf the prey. Trials were analysed in Windows Media Player (Microsoft).

Squid strike distance. Three to five squid were placed into a ~28 l acrylic tank with a quarter-inch bed of fine black sand. The tank was illuminated from the side with a panel of SMD3528-300-IR infrared (850 nm) LED light strip lights. An infrared camera (SiOnyx Aurora) fitted with an 850 nm infrared filter (Neewer) was mounted above the tank to record for the full duration of the trial. Two conditions were filmed, one with overhead room lights turned on to full brightness, and one with the room in total darkness. Trials started at 10:00 and ended once all shrimp had been eaten or at 17:00—whichever happened first. Five to ten shrimp were added to the tank at 10:00 and the camera was activated. Once the trial had completed, still frames of the video were extracted into ImageJ (NIH) and analysed to measure distance to prey and striking angle using known measurements to calibrate the ImageJ measuring tool. Videos were also analysed in ImageJ to determine the success and failure proportion of every strike made during the duration of the trial for both light and dark trials.

Octopus/squid versus prey movement. Trials from squid strike distance were analysed in ImageJ using the Trackmate[55] plugin to quantify distance travelled (in cm) of both the shrimp and the squid for 15 s before a successful strike. Prey capture trials for octopus were performed in a ~190 l tank prepared in a room with full lighting control and filmed top-down with a GO-PRO HERO7 (GoPro) camera. A live fiddler crab was placed on one side of the tank, and an octopus was placed on the opposite side of the tank. Trials were recorded for 15 s and always resulted in successful prey capture. Videos were analysed in ImageJ (NIH) using the Trackmate plugin to quantify distance travelled (cm) of both the octopus and the crab.

Squid prey handling time. Squid were offered shrimp tied to fishing line (Stren monofilament fishing line, ~13.6 kg test weight) in their home tank. The shrimps were soaked in a 1 l solution of either seawater or 1 mM denatonium for 2 h before being offered to the squids. Handling time was measured as the time spent with arms actively manipulating the prey item, as opposed to the stereotypic consumption behaviour consisting of holding the arms in a resting posture entirely engulfing the prey item. Trials were recorded using a GO-PRO HERO7 (GoPro) in normal room lighting and analysed using Windows Media Player (Microsoft).

Two-choice assay. A ~28 l tank was prepared in a room with full lighting control and suspended 4 feet off the ground on a quarter-inch-thick sheet of clear acrylic to enable bottom-up filming with an infrared camera (SiOnyx Aurora) fitted with an 850 nm infrared filter (Neewer). The tank was illuminated both with overhead room lights and with a panel of SMD3528-300-IR infrared (850 nm) LED light strip lights. To test the effects of chemicals on chemotactile sensation, 400 ml of 1.5% concentration agarose (Agarose RA, VWR Life Science) was added and solidified on the bottom of the tank floor. The agar floor was bisected widthwise, and one side was removed (alternated across trials). Then, 200 ml of 1.5% agarose infused with the indicated compounds was added to the empty half of the tank, resulting in a uniform depth of agar across the tank. The tank was filled with 10 l of seawater, the animals were added to freely explore the tank and the entire 10 min trial was recorded from the side with a GoPro HERO7 camera (GoPro), in addition to the bottom-up recording of the IR camera. The animal was then returned to its home tank for at least 24 h. Videos were imported into ImageJ (NIH) and thresholded colorimetrically to allow pixel-based analysis of the octopus arms contacting the agar floor.

Quantification and statistical analysis

Data were analysed using Clampfit (Axon Instruments), Prism (GraphPad) and represented as mean ± s.e.m. *n* values represent independent experiments for the number of cells/patches or behavioural trials. Data were considered to be significant if $P < 0.05$ using paired or unpaired two-tailed Student's *t*-tests, Wilcox tests or one- or two-way ANOVAs. All significance tests were justified considering the experimental design and we assumed normal distribution and variance, as is common for similar experiments. Animal behaviour experiments were randomized and performed blinded to chemical stimulation conditions. Sample sizes were chosen on the basis of the number of independent experiments required for statistical significance and technical feasibility.

Reporting summary

Further information on research design is available in the Nature Portfolio Reporting Summary linked to this article.

Data availability

Deep sequencing data are available via the Sequence Read Archive (SRA) repository under the BioProject accession code PRJNA906054. The *CRB1* nucleotide sequence is available under NCBI accession OQ301567. Atomic model coordinates and cryo-EM density maps for the CRB1 structure have been deposited at the PDB under accession code 8EIZ and at the Electron Microscopy Data Bank under accession code EMD-28167, respectively.

18. Morales-Perez, C. L., Noviello, C. M. & Hibbs, R. E. Manipulation of subunit stoichiometry in heteromeric membrane proteins. *Structure* **24**, 797–805 (2016).
19. Zivanov, J. et al. New tools for automated high-resolution cryo-EM structure determination in RELION-3. *eLife* **7**, e42166 (2018).
20. Zheng, S. Q. et al. MotionCor2: anisotropic correction of beam-induced motion for improved cryo-electron microscopy. *Nat. Methods* **14**, 331–332 (2017).
21. Zhang, K. Gctf: real-time CTF determination and correction. *J. Struct. Biol.* **193**, 1–12 (2016).
22. Wagner, T. et al. SPHIRE-crYOLO is a fast and accurate fully automated particle picker for cryo-EM. *Commun. Biol.* **2**, 218 (2019).
23. Pettersen, E. F. et al. UCSF Chimera—a visualization system for exploratory research and analysis. *J. Comput. Chem.* **25**, 1605–1612 (2004).
24. Kucukelbir, A., Sigworth, F. J. & Tagare, H. D. Quantifying the local resolution of cryo-EM density maps. *Nat. Methods* **11**, 63–65 (2014).
25. Afonine, P. V. et al. New tools for the analysis and validation of cryo-EM maps and atomic models. *Acta Crystallogr. D* **74**, 814–840 (2018).
26. Morin, A. et al. Collaboration gets the most out of software. *eLife* **2**, e01456 (2013).
27. Waterhouse, A. et al. SWISS-MODEL: homology modelling of protein structures and complexes. *Nucleic Acids Res.* **46**, W296–W303 (2018).
28. Emsley, P., Lohkamp, B., Scott, W. G. & Cowtan, K. Features and development of Coot. *Acta Crystallogr. D* **66**, 486–501 (2010).
29. Adams, P. D. et al. PHENIX: a comprehensive Python-based system for macromolecular structure solution. *Acta Crystallogr. D* **66**, 213–221 (2010).
30. Liebschner, D. et al. Macromolecular structure determination using X-rays, neutrons and electrons: recent developments in Phenix. *Acta Crystallogr. D* **75**, 861–877 (2019).
31. Williams, C. J. et al. MolProbity: more and better reference data for improved all-atom structure validation. *Protein Sci.* **27**, 293–315 (2018).
32. Pettersen, E. F. et al. UCSF ChimeraX: structure visualization for researchers, educators, and developers. *Protein Sci.* **30**, 70–82 (2021).
33. The PyMOL Molecular Graphics System v.2.4.1 (Schrodinger, 2015).
34. UniProt, C. UniProt: a worldwide hub of protein knowledge. *Nucleic Acids Res.* **47**, D506–D515 (2019).
35. Pei, J., Kim, B. H. & Grishin, N. V. PROMALS3D: a tool for multiple protein sequence and structure alignments. *Nucleic Acids Res.* **36**, 2295–2300 (2008).
36. Smart, O. S., Neduvelil, J. G., Wang, X., Wallace, B. A. & Sansom, M. S. HOLE: a program for the analysis of the pore dimensions of ion channel structural models. *J. Mol. Graph.* **14**, 354–360 (1996).
37. Klesse, G., Rao, S., Sansom, M. S. P. & Tucker, S. J. CHAP: a versatile tool for the structural and functional annotation of ion channel pores. *J. Mol. Biol.* **431**, 3353–3365 (2019).
38. Krissinel, E. & Henrick, K. Inference of macromolecular assemblies from crystalline state. *J. Mol. Biol.* **372**, 774–797 (2007).
39. Tian, W., Chen, C., Lei, X., Zhao, J. & Liang, J. CASTp 3.0: computed atlas of surface topography of proteins. *Nucleic Acids Res.* **46**, W363–W367 (2018).
40. Grabherr, M. G. et al. Full-length transcriptome assembly from RNA-seq data without a reference genome. *Nat. Biotechnol.* **29**, 644–652 (2011).
41. Bray, N. L., Pimentel, H., Melsted, P. & Pachter, L. Near-optimal probabilistic RNA-seq quantification. *Nat. Biotechnol.* **34**, 525–527 (2016).
42. Buchfink, B., Reuter, K. & Drost, H. G. Sensitive protein alignments at tree-of-life scale using DIAMOND. *Nat. Methods* **18**, 366–368 (2021).
43. Eddy, S. R. Profile hidden Markov models. *Bioinformatics* **14**, 755–763 (1998).
44. Madden, T. in *The NCBI Handbook* 2nd edn (eds McEntyre, J. & Ostell, J.) Ch. 16 (2002).
45. Li, W. & Godzik, A. Cd-hit: a fast program for clustering and comparing large sets of protein or nucleotide sequences. *Bioinformatics* **22**, 1658–1659 (2006).
46. Katoh, K. & Standley, D. M. MAFFT multiple sequence alignment software version 7: improvements in performance and usability. *Mol. Biol. Evol.* **30**, 772–780 (2013).
47. Kalyaanamoorthy, S., Minh, B. Q., Wong, T. K. F., von Haeseler, A. & Jermiin, L. S. ModelFinder: fast model selection for accurate phylogenetic estimates. *Nat. Methods* **14**, 587–589 (2017).
48. Minh, B. Q. et al. IQ-TREE 2: new models and efficient methods for phylogenetic inference in the genomic era. *Mol. Biol. Evol.* **37**, 1530–1534 (2020).
49. Hoang, D. T., Chernomor, O., von Haeseler, A., Minh, B. Q. & Vinh, L. S. UFBoot2: improving the ultrafast bootstrap approximation. *Mol. Biol. Evol.* **35**, 518–522 (2018).
50. Dos Reis, M. & Yang, Z. Bayesian molecular clock dating using genome-scale datasets. *Methods Mol. Biol.* **1910**, 309–330 (2019).
51. Tanner, A. R. et al. Molecular clocks indicate turnover and diversification of modern coleoid cephalopods during the Mesozoic Marine Revolution. *Proc. R. Soc. B* **284**, 20162818 (2017).
52. Yu, G., Smith, D. K., Zhu, H., Guan, Y. & Lam, T. T.-Y. ggtree: an R package for visualization and annotation of phylogenetic trees with their covariates and other associated data. *Methods Ecol. Evol.* **8**, 28–36 (2017).
53. Revell, L. J. phytools: an R package for phylogenetic comparative biology (and other things). *Methods Ecol. Evol.* **3**, 217–223 (2012).
54. Suyama, M., Torrents, D. & Bork, P. PAL2NAL: robust conversion of protein sequence alignments into the corresponding codon alignments. *Nucleic Acids Res.* **34**, W609–W612 (2006).
55. Tinevez, J.-Y. et al. TrackMate: An open and extensible platform for single-particle tracking. *Methods* **15**, 80–90 (2017).
56. Jurrus, E. et al. Improvements to the APBS biomolecular solvation software suite. *Protein Sci.* **27**, 112–128 (2018).
57. Jumper, J. et al. Highly accurate protein structure prediction with AlphaFold. *Nature* **596**, 583–589 (2021).

Acknowledgements We thank C. Winkler for providing octopuses; B. Grasse of the Cephalopod Program and the Marine Resource Center at the MBL for squid; B. Walsh for animal husbandry; C. Heacock for help with nerve recordings; R. Lines for assistance with behavioural experiments; A. Grearson for photographs and illustrations; S. Burke for contributions to early stages of the project; J. Teng for preliminary functional tests; R. Cabuco and L. Baxter for baculovirus production; and C. Noviello for screening grids. Single-particle cryo-EM grids were screened at the University of Texas Southwestern Medical Center Cryo-Electron Microscopy Facility, which is supported by the CPRIT Core Facility Support Award RP170644. A portion of this research was supported by NIH grant U24GM129547 and performed at the PNCC at OHSU and accessed through EMSL (grid.436923.9), a DOE Office of Science User Facility sponsored by the Office of Biological and Environmental Research. This research was further supported by grants to N.W.B. from the New York Stem Cell Foundation, Searle Scholars Program and the NIH (R35GM142697 and R01NS129060); NIH grants to R.E.H. (R01NS120496 and R01NS129060) and to G.K. (F32DA047848); and support from the American Heart Association to J.J.K. (20POST35200127) and from the National Science Foundation to C.A.H.A. (NSF-PRFB 2010728).

Author contributions C.A.H.A., W.A.V.-M., L.v.G., P.B.K. and N.W.B. contributed to molecular, cellular and organismal studies. G.K., J.J.K., X.B. and R.E.H. contributed to biochemical and structural analyses. All of the authors were involved with writing or reviewing the manuscript.

Competing interests The authors declare no competing interests.

Additional information

Supplementary information The online version contains supplementary material available at https://doi.org/10.1038/s41586-023-05808-z.

Correspondence and requests for materials should be addressed to Nicholas W. Bellono or Ryan E. Hibbs.

Peer review information *Nature* thanks Hugues Nury, Oleg Simakov and Harold Zakon for their contribution to the peer review of this work. Peer reviewer reports are available.

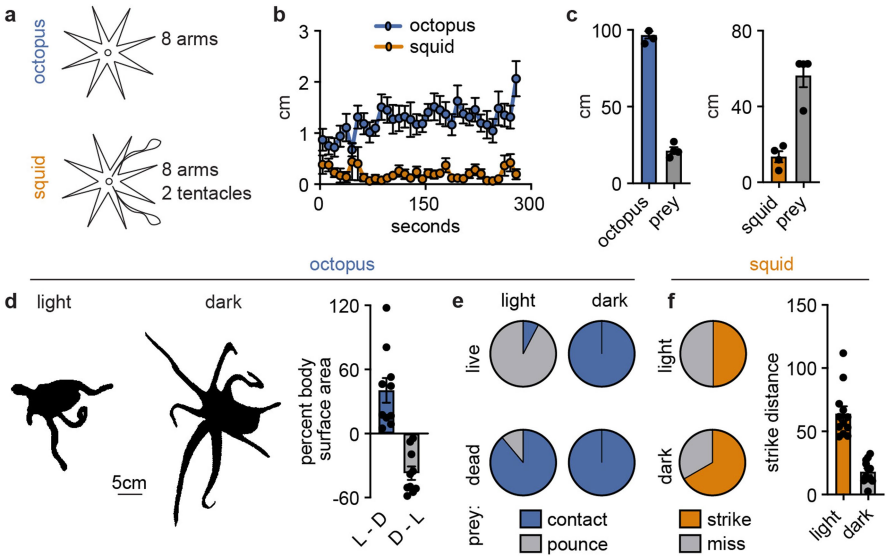

Extended Data Fig. 1 | Comparative chemotactile behaviour. a, Squid have two long tentacles for catching prey, in addition to eight arms like octopus. **b**, Octopuses explore their home tank, moving throughout recordings while squid are stationary and often buried. n = 8-9 trials. **c**, Octopuses move toward their prey for capture while squid wait for prey to approach and then strike. n = 4 trials, $p < 0.0001$ for octopus versus squid movement, two-tailed Student's t-test. **d**, Octopuses spread their arms in relatively dark conditions and contract in the light. n = 10 trials, $p < 0.0001$ for octopus versus squid movement, two-tailed Student's t-test. **e**, Octopuses pounce on and consume live crabs from a distance in the light and must first touch freshly dead crabs before consuming. In the dark, octopuses must first touch live or dead crabs before pouncing and consuming. These results suggest octopuses use somatosensation for predation in the absence of strong visual cues. n = 9–13 trials. **f**, Squid use ambush predation to hide and strike shrimp in light or relatively dark conditions with a similar success rate but require that prey are at a much closer distance in the dark. These results suggest squid primarily use vision to strike prey. $p < 0.0001$ for strike distance in light versus dark, two-tailed Student's t-test. n = 18–24 trials. Data represented as mean ± SEM.

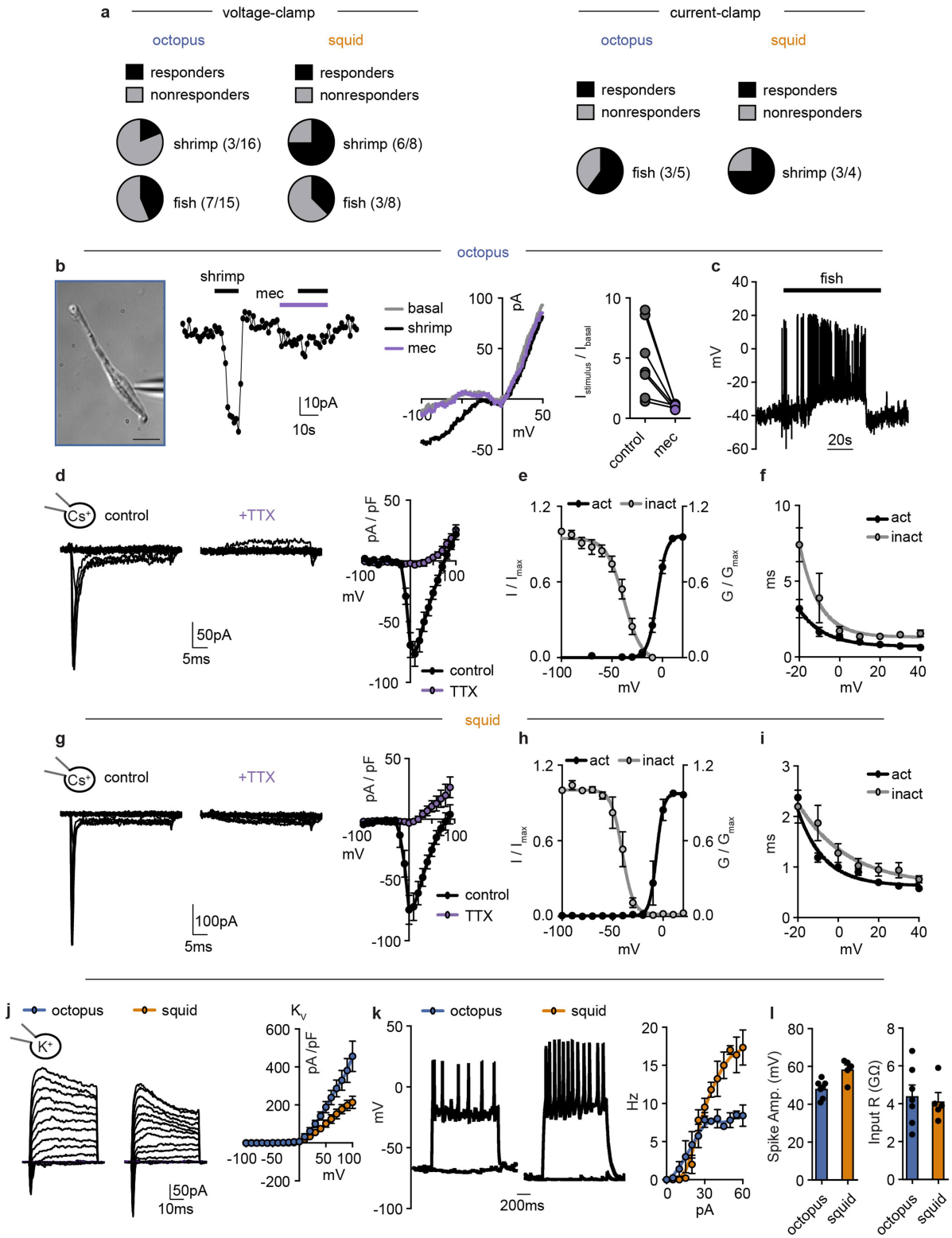

Extended Data Fig. 2 | See next page for caption.

Extended Data Fig. 2 | Comparative chemosensory cell electrical properties. a, Quantification of chemosensory cells from octopus or squid that responded to 3 kDa fish and shrimp extract in voltage- or current-clamp. **b**, Shrimp-sensitive octopus chemoreceptor cell currents were blocked by 1 mM mecamylamine. $p < 0.05$, two-tailed Student's t-test. n = 7 cells. Scale bar: 5 µm. **c**, Representative fish-evoked action potentials in an octopus chemosensory cell. **d**, 1 µM tetrodotoxin (TTX) blocked voltage-gated inward currents (I_{Nav}) in octopus chemosensory cells. n = 6-11 cells, $p < 0.0001$, two-way ANOVA with post hoc Bonferroni test. **e**, Octopus chemosensory cell I_{Nav} voltage dependence: $V_{a1/2} = -5.1 \pm 0.7$ mV, $V_{i1/2} = -38.0 \pm 1.8$ mV, n = 4. **f**, Octopus chemosensory cell I_{Nav} activation and inactivation kinetics. n = 6. **g**, 1 µM tetrodotoxin (TTX) blocked voltage-gated inward currents (I_{Nav}) in squid chemosensory cells. n = 6–11 cells, $p < 0.0001$, two-way ANOVA with post hoc Bonferroni test. **h**, Squid chemosensory cell I_{Nav} voltage dependence: $V_{a1/2} = -6.5 \pm 0.8$ mV, $V_{i1/2} = -40.3 \pm 1.3$ mV, n = 4 cells. **i**, Squid chemosensory cell I_{Nav} activation and inactivation kinetics. n = 6 cells. **j**, Voltage-gated outward currents measured in the presence of intracellular potassium (I_{KV}) in squid and octopus chemosensory cells. n = 5 cells for squid and 6 for octopus. **k**, Both squid and octopus chemosensory cells produced action potentials in response to current injection. Squid had slightly higher frequency in response to the same injection step. n = 5 cells for squid and 7 for octopus. **l**, comparison of spike amplitude and input resistance in squid and octopus chemosensory cells. n = 5 cells for squid and 7 for octopus. Data represented as mean ± SEM.

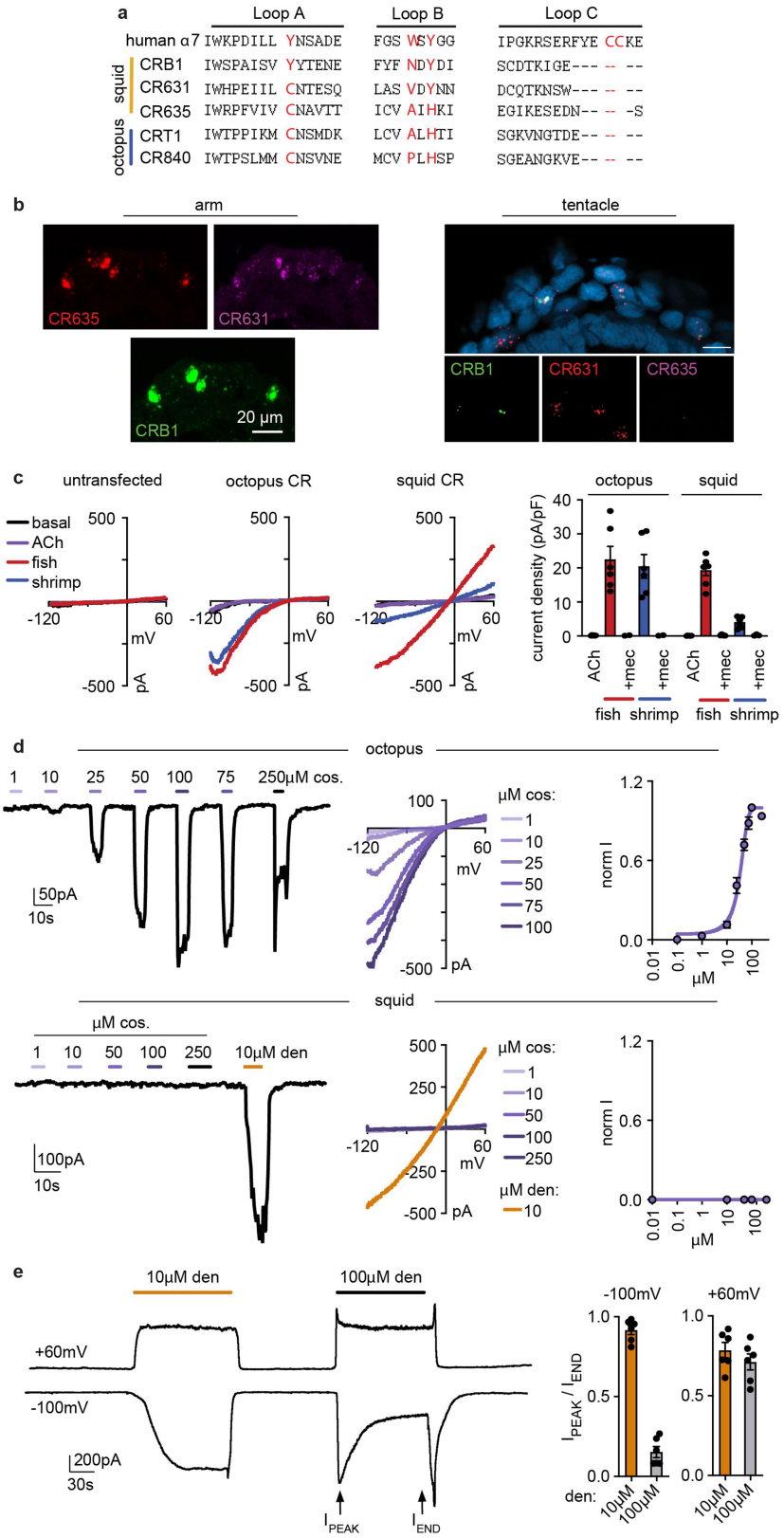

Extended Data Fig. 3 | See next page for caption.

Extended Data Fig. 3 | Squid CR properties. a, Alignment of predicted loops A, B and C from analysed octopus and cuttlefish CRs and the human α7 nicotinic acetylcholine receptor demonstrated that CRs lack most residues that contribute to the canonical acetylcholine (ACh) binding side (highlighted in red). **b**, Squid CRs localized to the sensory epithelium of arm suckers (*left*, merge in Fig. 1) and tentacle suckers (*right*), as visualized by RNAscope *in situ* hybridization. Nuclei were stained with DAPI (blue). Representative of 3 animals. **c**, Expressed octopus (CR518, CRT1) and cuttlefish CRs (CR192, CRB1) were insensitive to acetylcholine (ACh, 1 mM) but robustly responded to fish or shrimp extract. Extract responses were blocked by mecamylamine (1 mM) and were not observed in untransfected cells. n = 6–7 cells, $p < 0.0001$ for extract responses versus mecamylamine, two-way ANOVA with post-hoc Tukey test. **d**, Octopus CRT1 exhibited dose-dependent sensitivity to the terpene costunolide, while squid CRB1 was insensitive. Octopus CRT1 EC50 = 30.8 μM, 95% CI = 30.0 – 33.9 μM, n = 7 cells for octopus and 5 for squid. Data represented as mean ± SEM. **e**, Minimal desensitization was measured in response to low concentration of denatonium while higher concentrations produced inhibition with large wash-off currents that were absent at positive voltage. These properties are consistent with moderate pore block. $p < 0.0001$ for concentration, two-tailed student's t-test (n = 6). Data represented as mean ± SEM.

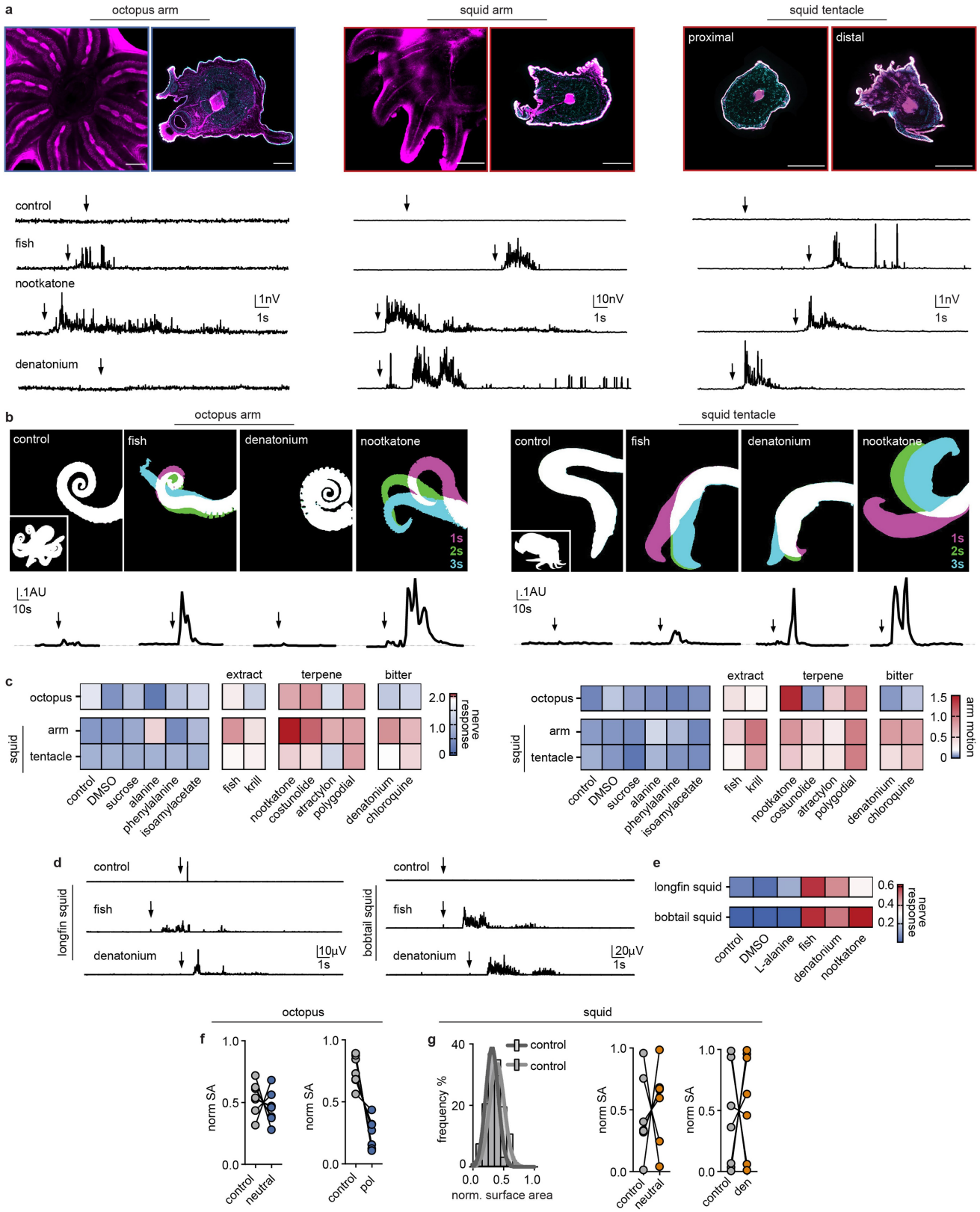

Extended Data Fig. 4 | See next page for caption.

Extended Data Fig. 4 | Comparative squid and octopus nerve and arm chemosensory responses. a, (*Top*) arm and tentacle axial nerves stained with anti-horseradish peroxidase antibody (purple) and nuclear stain (DAPI, blue). Representative of at least 3 animals. Scale bars: 1 mm. (*Bottom*) Corresponding nerve recordings in response to the indicated stimuli: control (sea water), 3 kDa fish extract, 1 mM nootkatone, 1 mM denatonium. **b**, Amputated arm behaviour in response to control (sea water), 3 kDa fish extract, 1 mM denatonium, or 1mM nootkatone. **c**, Heat map of normalized axial nerve and arm responses. Octopus and squid were sensitive to terpenes but only squid arms and tentacles responded to denatonium. $p < 0.05$ for denatonium sensitivity in squid, $n = 3$ arms. **d**, Representative axial nerve recordings from longfin (*D. pealii*) and bobtail squid (*E. berryi*) arms in response to control (sea water), 3 kDa fish extract, 1 mM denatonium. **e**, Heat map of normalized axial nerve responses in longfin and bobtail squid. **f**, Normalized surface area of octopus arms touching agar coated floors was reduced on the side containing polygodial (100 μM, $n = 7$). Octopuses touched both control sides the same. $p < 0.01$, paired Student's t test, $n = 8$ trials per condition. **g**, Squid touched agar-coated floors with the same frequency and surface area when both sides were coated with sea water-filled agar or one side contained denatonium (also see Fig. 2). $n = 7$ trials.

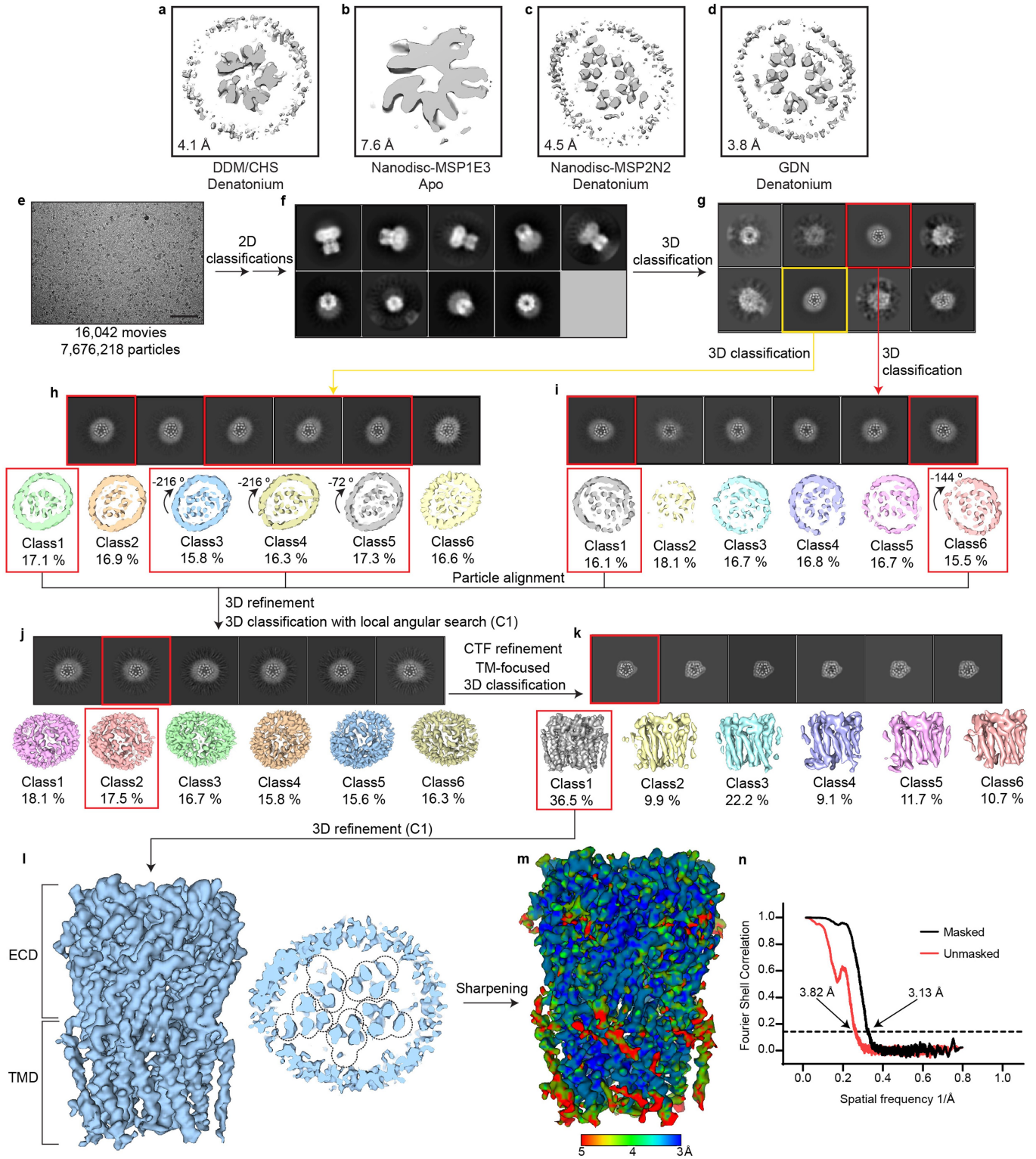

Extended Data Fig. 5 | EM data processing. a-d, 2D slices through TMDs from reconstructions of CRB1 in different membrane mimetics. **e**, Representative cryo-electron micrograph of CRB1 in GDN detergent micelles from a dataset of 16,042 dose-fractionated micrographs. Scale bar = 100 nm. **f**, Projection images from the selected 2D classes. **g**, 3D classification results; good 3D classes selected for separate processing are boxed in red and yellow. **h-i**, 3D classification results; 3D classes selected are boxed in red, and particles from selected 3D classes were aligned and combined for 3D refinement. **j**, 3D classification results using local angular searches; best 3D class with strong TMD density boxed in red was selected for additional 3D classification. **k**, TMD-focused 3D classification results; particles from best 3D class (boxed in red) were used in final refinement. **l**, 3D reconstructed map from the final 3D classification, which is shown in both side and top views. Density of M1-M4 for each subunit is outlined with a black dashed line. **m**, Sharpened map coloured by local resolution. **n**, Half-map FSC plot for masked and unmasked maps with global resolution indicated at FSC = 0.143.

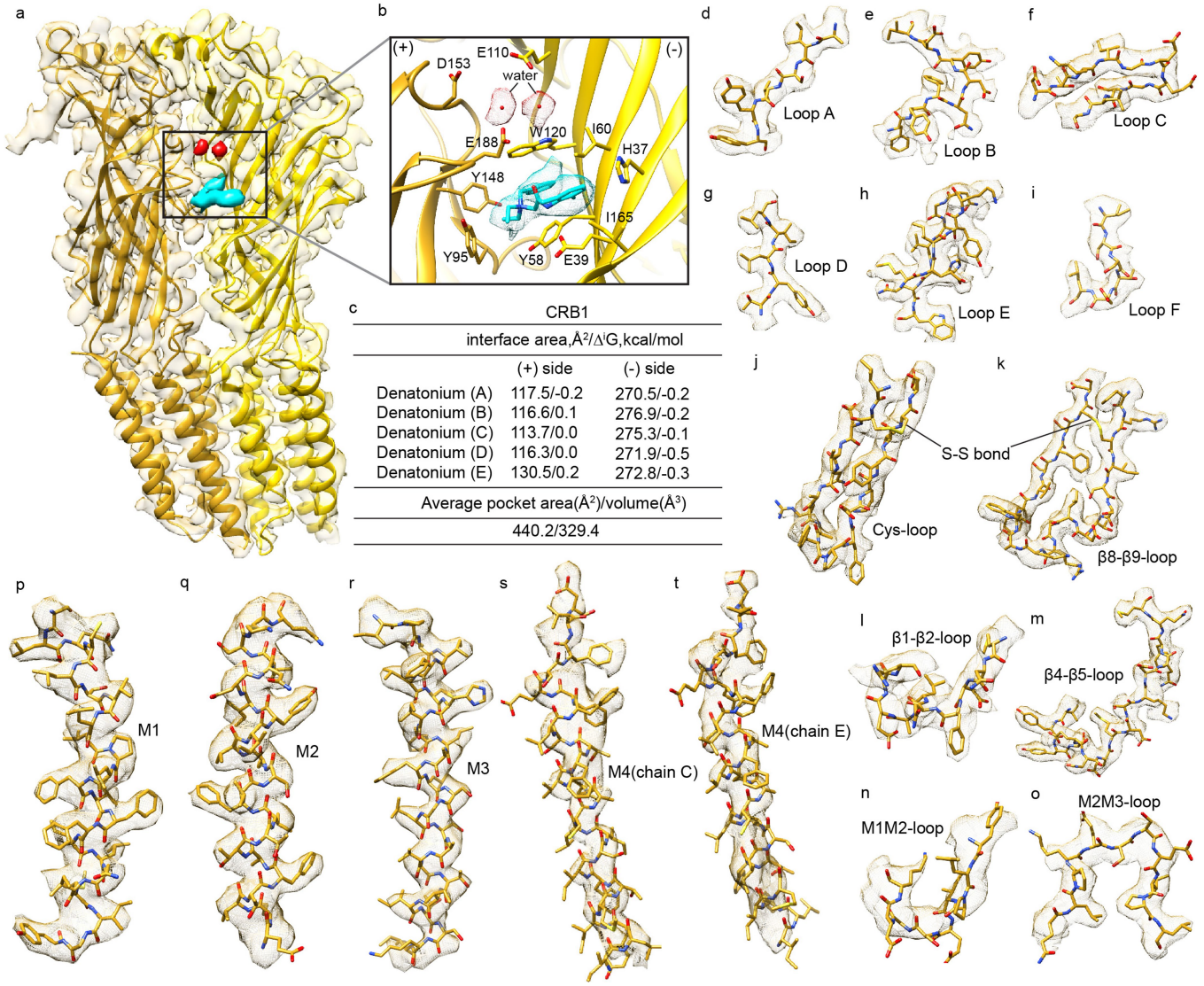

Extended Data Fig. 6 | Representative density map segmentation. **a**, Cryo-EM density map of CRB1 for representative adjacent subunits coloured in gold and yellow. Density map of denatonium coloured in cyan and waters in red at a threshold level of 0.03. **b**, Orthosteric binding site of CRB1 boxed in **a**, where residues within 5 Å of denatonium and negatively charged residues near waters are shown as sticks. **c**, Calculated interface areas and interaction energies ($\Delta^{i}G$) for protein and denatonium using PDBePISA[38]. Calculated solvent accessible area and volume of the binding pocket for CRB1 using CASTp3.0[39]. **d**–**i**, Cryo-EM density segments of Loops A-F at the orthosteric binding site at a threshold level of 0.03. **j**–**o**, Cryo-EM density segments of Cys-loop, β8-β9-loop, β1-β2-loop, β4-β5-loop, M1M2 loop, and M2M3 loop at a threshold level of 0.03. **p**–**t**, Cryo-EM density segments of M1-M3 and two M4 helices (chains C and E) at a threshold level of 0.03.

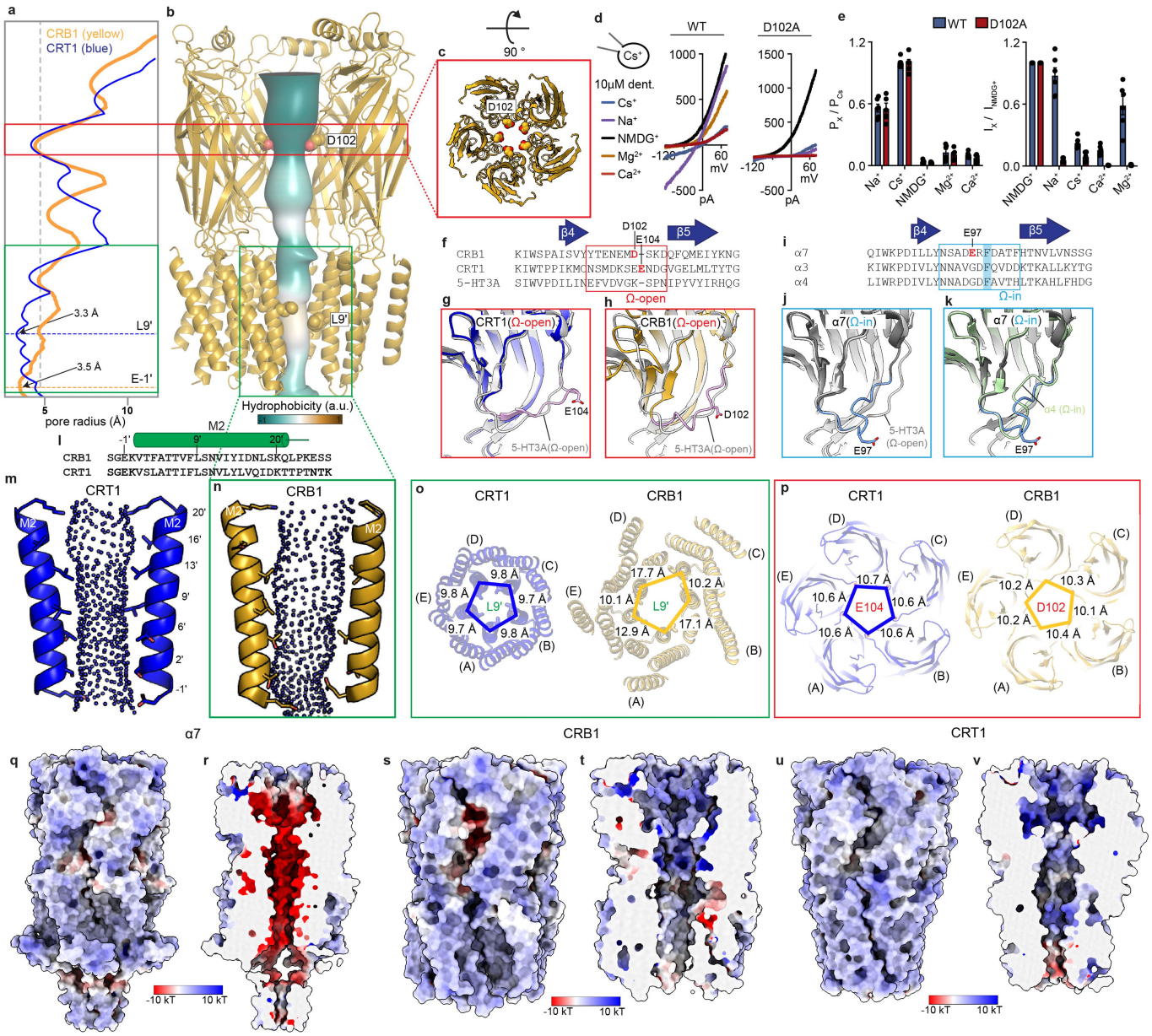

Extended Data Fig. 7 | Squid CR ion permeation pathway. a, Pore radii as a function of distance along the pore axis; CRB1 is coloured in yellow and CRT1 in blue. Structures were aligned using the M2 helix Glu-1′ at the bottom of M2, which is defined as y = 0. **b**, CRB1 ion permeation pathway coloured by hydrophobicity[37] with D102 and F46 indicated as spheres, the two most constricted points in the ECD; front subunit removed for clarity. **c**, Top view of CRB1 shows negatively charged D102 points toward the channel axis. **d**, Representative current-voltage (I-V) relationships of WT and D102A mutant CRB1 channels in response to denatonium during equimolar cation substitution. **e**, D102A did not change permeation but did affect current amplitude measured at +60 mV in the presence of all permeant cations. Outward currents in external $NMDG^+$ were the same in WT versus D102A. n = 7–10 cells, $p < 0.0001$ two-way ANOVA with post-hoc Bonferroni test. Data represented as mean ± SEM. **f**, Structure-based sequence alignment of β4-β5 loop (Ω loop) for CRB1, CRT1, and 5-HT_{3A} (PDB: 6NP0). **g**, Comparison of Ω loop conformation of CRB1 coloured in pink and 5-HT_{3A} (Ω-open) coloured in grey; D102 of CRB1 is shown as sticks. **h**, Comparison of Ω loop conformation of CRT1 coloured in pink and 5-HT_{3A} (Ω-open) coloured in grey; E104 of CRT1 is shown as sticks. **i**, Structure-based sequence alignment of Ω loop for α7 (PDB: 7KOX), α3 (PDB: 6PV7), α4 nicotinic receptor (PDB: 5KXI). **j**, Comparison of Ω loop conformation of α7 nicotinic receptor coloured in light blue and 5-HT_{3A} (Ω-open) coloured in grey; E97 of α7 is shown as sticks. **k**, Comparison of Ω loop conformation of α7 nicotinic receptor coloured in light blue and α4 nicotinic receptor (Ω-in) coloured in light green. **m**,**n**, Comparison of pore shapes analysed by HOLE2[36]. **o**,**p**, Comparison of relative symmetry in the TMD (**o**) and ECD (**p**) for CRT1 and CRB1. **q**,**r**, α7 receptor electrostatics analysed by APBS[56], where **r** is a cutaway to show electrostatics of the permeation pathway, calculated with 140 mM NaCl. **s**–**v**, Electrostatics for CRB1 and CRT1, calculated with 0.5 M NaCl.

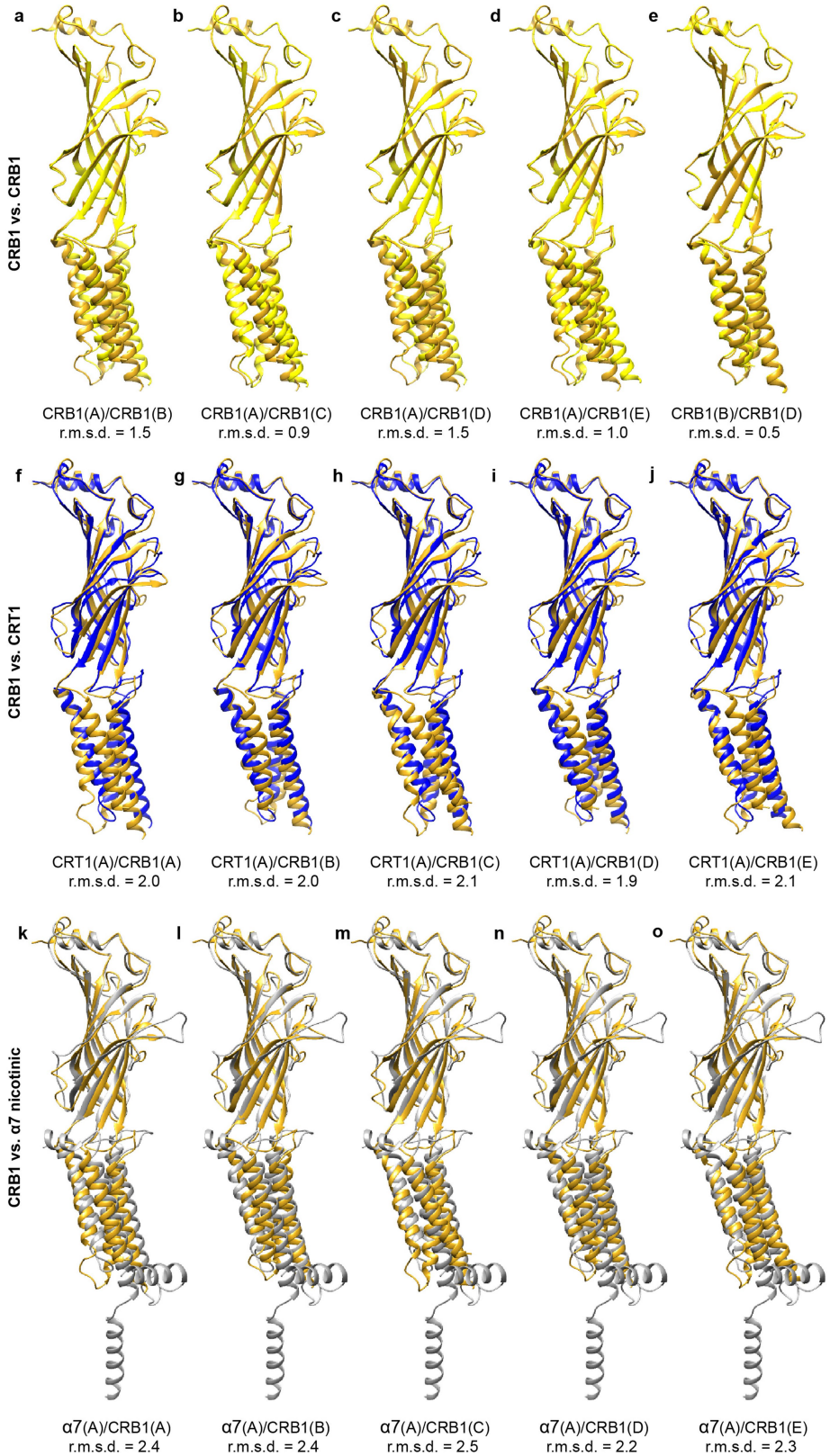

Extended Data Fig. 8 | Superposition of subunits from CRs and α7 nicotinic receptor. a–e, Superposition of subunits within CRB1, aligned by ECD region using UCSF Chimera. The r.m.s.d values in Å are for Cα atoms over the whole chain, calculated by secondary structure-based alignment using Coot. Chain IDs are indicated in parentheses. **f–j**, Subunits of CRB1 are compared to a subunit of CRT1. **k–o**, Subunits of CRB1 are compared to a subunit of α7 nicotinic receptor (activated state, PDB:7KOX).

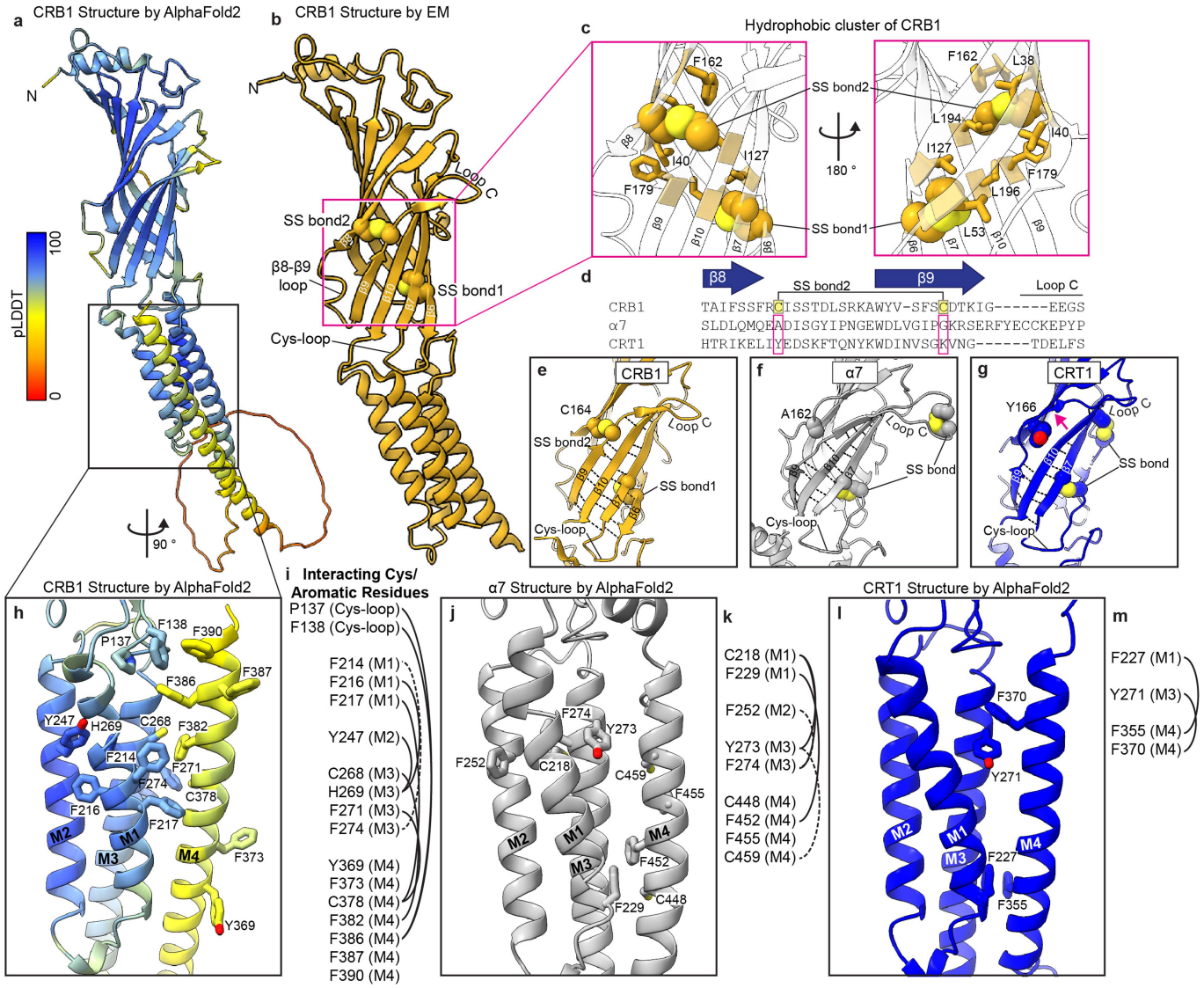

Extended Data Fig. 9 | Squid CR hydrophobic cluster and hydrogen bond network. a, Single subunit structure of squid CR predicted by AlphaFold[57] and coloured by confidence. **b**, Experimental cryo-EM structure of single subunit with two disulfide bonds shown as spheres. **c**, Details of CRB1 boxed in **b**, and a 180° rotated view. Hydrophobic residues contacting the two disulfide bonds are shown as sticks. **d**, Structure-based sequence alignment of β8-β9 loop and Loop C of CRB1, CRT1, and human α7 nicotinic acetylcholine receptor. A novel disulfide bond in CRB1 is highlighted in a yellow box, and the corresponding residue on the β8-β9 loop in CRT1 and α7 is indicated in a magenta-coloured box. **e**, Hydrogen bond network between β9, β10, β7 and β6 in CRB1 shown as black dashed line. **f**, Hydrogen bond network between β9, β10, and β7 in CRT1 at the same view as **e**. The β9 strand shifts upward as indicated by the magenta arrow due to insertion of the Y166 sidechain between β9 and β10, which breaks the hydrogen bond network in this region. **g**, Hydrogen bond network between β9, β10, and β7 in α7 in the same orientation as **e**. **h**-**m**, In the TMD, density for the most peripheral M4 helix was notably absent in CRT1, in all tested detergents, but it was predicted to be present by AlphaFold. **h**, **j**, and **l** show predicted structures of TMD bundles for CRB1, α7, and CRT1. **i**, **k**, and **m** show interactions as lines from PDBePISA server analysis; solid lines indicate interactions found in both the experimental structures and in the AlphaFold model; dashed lines indicate those found in only the experimental structures. In panel **m**, solid lines indicate interactions found only in the AlphaFold model. Analysis of molecular interactions among M1/M3/M4 helices from the experimental and predicted models sheds light on the basis for the presence or absence of an ordered M4 helix. In CRB1 and α7, plentiful aromatic contacts among helices stabilize M4 packing in the TMD bundle, while the most recently diverged CRT1 lacks the abundance of hydrophobic contacts.

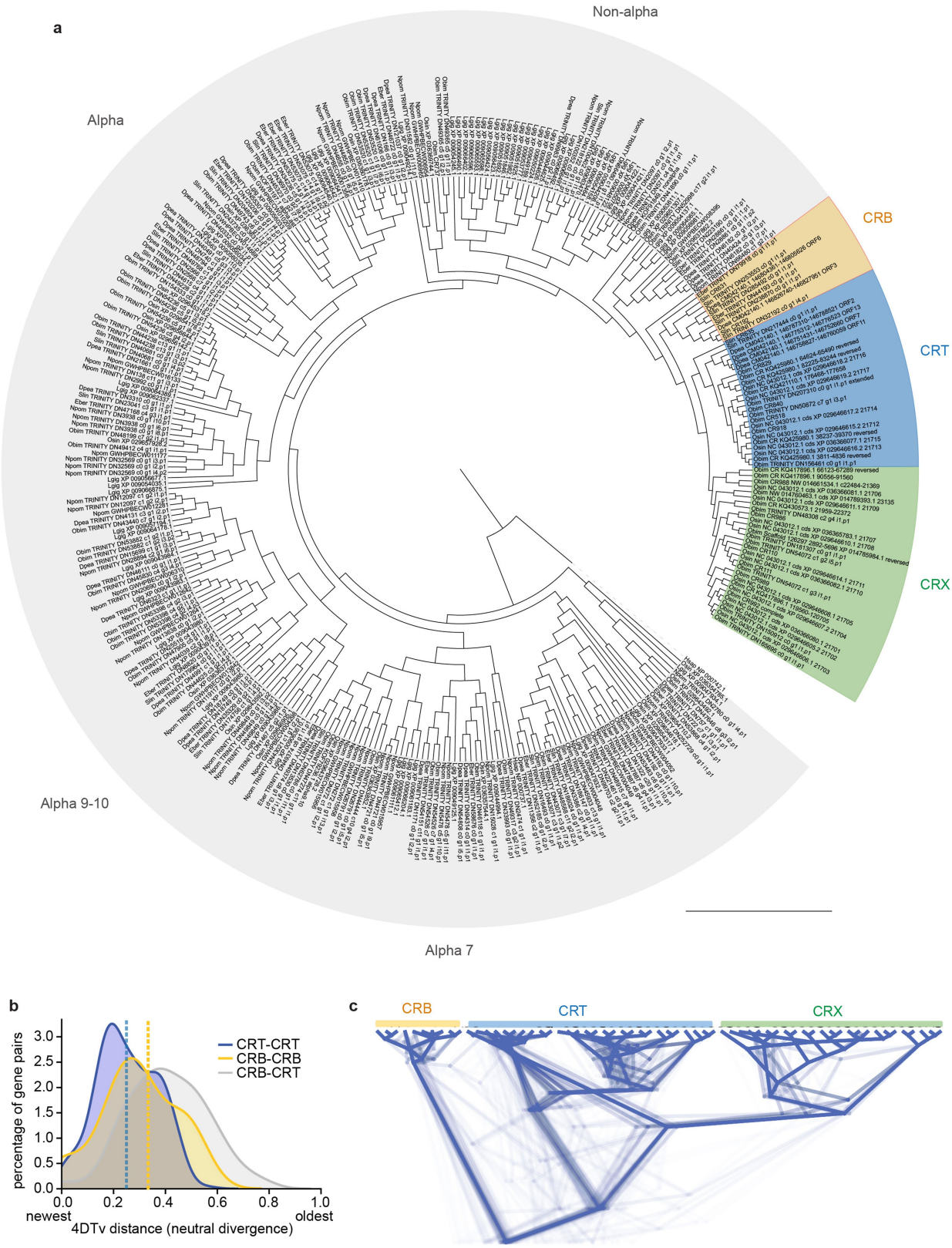

Extended Data Fig. 10 | Comparative squid and octopus CR phylogeny. **a**, Phylogenetic tree of acetylcholine-receptor-like protein sequences from *Octopus bimaculoides* (Obim), *Octopus sinensis* (Osin), *Sepioloidea lineolata* (Slin), *Doryteuthis pealeii* (Dpea), *Euprymna berryi* (Eber), *Nautilus pompilius* (Npom), and *Lottia gigantea* (Lgig) showing that CRs diverged from acetylcholine-like receptors, are unique to coleoid cephalopods, and comprise three major lineages: CRB (CR-Bitter), CRT (CR-Terpenes), and CRX (CR with unknown ligands). **b**, Density distributions of neutral genetic diversity (fourfold degenerate site distances, 4DTv) estimated for all pairs of genes between CRB and CRT clades. Dotted lines correspond to the mode of distributions for pairwise comparisons between CRTs and CRBs, suggesting CRTs have undergone a more recent diversification. **c**, Densitree of the distribution of bootstrap topologies for the CR clade showing that CRB is robustly supported as the earliest divergent lineage of CRs and sister to the CRT-CRX clade.

Extended Data Table 1 | Cryo-EM data collection, processing, and model statistics

	Denatonium CRB1, GDN (EMD-28167, PDB 8EIZ)
Data collection and processing	
EM Facility	PNCC
Magnification	81000
Voltage (kV)	300
Electron exposure ($e^-/Å^2$)	50
Defocus range (μm)	-0.5 to -2.5
Pixel size (Å)	1.069
Symmetry imposed	C1
Initial particle images (no.)	7,676,218
Final particle images (no.)	70,869
Map resolution (Å)	3.13
FSC threshold	0.143
Map sharpening B factor ($Å^2$)	-90
Refinement	
Initial model used (PDB code)	6PV7
Model Composition	
Non-hydrogen atoms	26415
Protein residues	1575
N-glycan	15
Denatonium	5
Water	10
B factors ($Å^2$)	
Protein	81.99
Ligand	79.45
Water	39.84
R.m.s. deviations	
Bond length ($Å^2$)	0.006
Bond angle (°)	0.690
Validation	
Molprobity score	1.61 (100^{th} %)
Clashscore	5.87 (100^{th} %)
Poor rotamers (%)	0.00
Ramachandran plot	
Favored (%)	95.76
Allowed (%)	4.24
Outliers (%)	0.00

nature portfolio

Corresponding author(s): Ryan E. Hibbs, Nicholas W. Bellono

Last updated by author(s): Jan 19, 2023

Reporting Summary

Nature Portfolio wishes to improve the reproducibility of the work that we publish. This form provides structure for consistency and transparency in reporting. For further information on Nature Portfolio policies, see our Editorial Policies and the Editorial Policy Checklist.

Statistics

For all statistical analyses, confirm that the following items are present in the figure legend, table legend, main text, or Methods section.

n/a	Confirmed
☐	☒ The exact sample size (*n*) for each experimental group/condition, given as a discrete number and unit of measurement
☐	☒ A statement on whether measurements were taken from distinct samples or whether the same sample was measured repeatedly
☐	☒ The statistical test(s) used AND whether they are one- or two-sided *Only common tests should be described solely by name; describe more complex techniques in the Methods section.*
☐	☒ A description of all covariates tested
☐	☒ A description of any assumptions or corrections, such as tests of normality and adjustment for multiple comparisons
☐	☒ A full description of the statistical parameters including central tendency (e.g. means) or other basic estimates (e.g. regression coefficient) AND variation (e.g. standard deviation) or associated estimates of uncertainty (e.g. confidence intervals)
☐	☒ For null hypothesis testing, the test statistic (e.g. *F*, *t*, *r*) with confidence intervals, effect sizes, degrees of freedom and *P* value noted *Give P values as exact values whenever suitable.*
☒	☐ For Bayesian analysis, information on the choice of priors and Markov chain Monte Carlo settings
☒	☐ For hierarchical and complex designs, identification of the appropriate level for tests and full reporting of outcomes
☒	☐ Estimates of effect sizes (e.g. Cohen's *d*, Pearson's *r*), indicating how they were calculated

Our web collection on statistics for biologists contains articles on many of the points above.

Software and code

Policy information about availability of computer code

Data collection	pClamp11
Data analysis	GraphPad Prism 9.5, Coot 0.8.9.3, Phenix 1.19.1-4122, Phenix 1.20.1-4487, Relion 3.1.2_cu9.2, Relion 3.1.3_cu10.2, MotionCor2, GCTF, crYOLO, Chimera 1.15, Chimera X, ResMap, Pymol 2.4.1, Hole2, CHAP

For manuscripts utilizing custom algorithms or software that are central to the research but not yet described in published literature, software must be made available to editors and reviewers. We strongly encourage code deposition in a community repository (e.g. GitHub). See the Nature Portfolio guidelines for submitting code & software for further information.

Data

Policy information about availability of data

All manuscripts must include a data availability statement. This statement should provide the following information, where applicable:

- Accession codes, unique identifiers, or web links for publicly available datasets
- A description of any restrictions on data availability
- For clinical datasets or third party data, please ensure that the statement adheres to our policy

Deep sequencing data are available via the Sequence Read Archive (SRA) repository under the accession code PRJNA906054. Atomic model coordinates and cryo-EM density maps for the CRB1 structure have been deposited in the Protein Data Bank with accession code 8EIZ and in the Electron Microscopy Data Bank with accession code EMD-28167, respectively.

Human research participants

Policy information about studies involving human research participants and Sex and Gender in Research.

Reporting on sex and gender	n/a
Population characteristics	n/a
Recruitment	n/a
Ethics oversight	n/a

Note that full information on the approval of the study protocol must also be provided in the manuscript.

Field-specific reporting

Please select the one below that is the best fit for your research. If you are not sure, read the appropriate sections before making your selection.

☒ Life sciences ☐ Behavioural & social sciences ☐ Ecological, evolutionary & environmental sciences

For a reference copy of the document with all sections, see nature.com/documents/nr-reporting-summary-flat.pdf

Life sciences study design

All studies must disclose on these points even when the disclosure is negative.

Sample size	Sample sizes were determined based on preliminary experiments and prior experiences of the investigators.
Data exclusions	RELION-based 2D and 3D classification of single particle datasets were used to remove junk particles.
Replication	All attempts at replication were successful as described in figure legends and methods.
Randomization	All experimental treatments were randomized. EM particle sets were randomly split to estimate overall resolution.
Blinding	Animal behavior experiments were blinded. Due to technical reasons, electrophysiological and structural analyses were not blinded, however results were near binary so we are confident they remain unbiased.

Reporting for specific materials, systems and methods

We require information from authors about some types of materials, experimental systems and methods used in many studies. Here, indicate whether each material, system or method listed is relevant to your study. If you are not sure if a list item applies to your research, read the appropriate section before selecting a response.

Materials & experimental systems

n/a	Involved in the study
☐	☒ Antibodies
☐	☒ Eukaryotic cell lines
☒	☐ Palaeontology and archaeology
☐	☒ Animals and other organisms
☒	☐ Clinical data
☒	☐ Dual use research of concern

Methods

n/a	Involved in the study
☒	☐ ChIP-seq
☒	☐ Flow cytometry
☒	☐ MRI-based neuroimaging

Antibodies

Antibodies used	1:500 anti-HRP-Cy3 (Jackson Immuno # 123-545-021)
Validation	This is a well established antibody for invertebrate neurons that was obtained from an established commercial source. We did not validate it further than visualized that it stains nerves and not other tissues.

Eukaryotic cell lines

Policy information about cell lines and Sex and Gender in Research

Cell line source(s)	HEK293: ATCC CRL-3022; Sf9: ATCC CRL-1711
Authentication	Purchased from commercial supplier. Not further tested.
Mycoplasma contamination	Not tested.
Commonly misidentified lines (See ICLAC register)	No commonly misidentified cells lines were used.

Animals and other research organisms

Policy information about studies involving animals; ARRIVE guidelines recommended for reporting animal research, and Sex and Gender in Research

Laboratory animals	Octopus bimaculoides (adult, 1-2 years), Sepioloidea lineolata (adult, 1-2 years), Euprymna berryi (adult, 1-2 years),
Wild animals	Doryteuthis pealeii (adult, 1-2 years) were caught by jigging at the MBL (Woods Hole, MA), transported in aerated coolers to Harvard University, and euthanized euthanized based on established methods with immersion of 3.5% MgCl2 and 15% ethanol followed by pithing.
Reporting on sex	Sex was not considered as a variable due to limited animal availability.
Field-collected samples	No
Ethics oversight	Animal protocols were approved by the Harvard University Animal Care and Use Committee (protocol ID 18-05-325).

Note that full information on the approval of the study protocol must also be provided in the manuscript.